Cryo-EM structure revealed a novel F-actin binding motif in a *Legionella pneumophila* lysine fatty-acyltransferase

Wenjie W. Zeng[a,b], Garrison Komaniecki[c,e], Jiaze Liu,[b,f] Hening Lin[c,d], and Yuxin Mao[a,b,1]

[a]Weill Institute for Cell and Molecular Biology, Cornell University, Ithaca, NY 14853, USA.

[b]Department of Molecular Biology and Genetics, Cornell University, Ithaca, NY 14853, USA.

[c]Department of Chemistry, Department of Molecular Biology and Genetics, Cornell University, Ithaca, NY 14853, USA

[d]Howard Hughes Medical Institute; Department of Medicine and Department of Chemistry, The University of Chicago, Chicago, IL 60637, USA

[e]Current address: Chemistry Department, University of Wisconsin – Parkside, Kenosha, WI 53406, USA.

[f]Current address: Department of Pharmacology, Yale University School of Medicine, New Haven, CT 06520, USA.

[1] Corresponding Author:

E-mail: ym253@cornell.edu

Telephone: 607-255-0783

Abstract

Legionella pneumophila is an opportunistic bacterial pathogen that causes Legionnaires' disease. To establish an intracellular niche conducive to replication, *L. pneumophila* translocates a diverse array of effector proteins that manipulate various host cellular processes, including the actin cytoskeleton. In a screen for effectors that alter actin dynamics, we identified a *Legionella* effector, Lfat1 (lpg1387), which colocalizes with the actin cytoskeleton in eukaryotic cells. Lfat1 specifically binds F-actin through a novel actin-binding domain (ABD). High-resolution cryo-electron microscopy (cryoEM) analysis revealed that this ABD forms a long α-helix hairpin, with its tip interacting with subdomains I and II of two adjacent actin molecules within the F-actin filament. Interestingly, while individual α-helices of the hairpin fail to bind F-actin, co-expression as separate fusion proteins restores binding activity. Furthermore, we demonstrated that Lfat1 exhibits lysine fatty-acyltransferase (KFAT) activity, targeting host small GTPases. These findings establish a foundation for studying the KFAT family of bacterial toxins and uncover a novel F-actin binding motif, providing an alternative F-actin marker with notable flexibility.

Introduction

The actin cytoskeleton plays an essential role in diverse cellular processes, including cell motility, cytokinesis, intracellular trafficking, and cell signaling (Dominguez & Holmes, 2011; Letort *et al*, 2015; Pollard, 2016). Actin is one of the most conserved, ubiquitous, and abundant proteins in cells from amoebas to humans (Pollard, 2016). Actin exists in two distinct forms: the monomeric G-actin form and the double-stranded filamentous F-actin form. F-actin is highly dynamic with a net association of ATP-actin to the barbed (+) end and dissociation of ADP-actin monomers from the pointed (-) end (Pollard, 2016). The assembly and disassembly of F-actin *in vivo* is intricately regulated through interactions with a structurally and functionally diverse family of Actin-Binding Proteins (ABPs) (Pollard, 2016). These actin-binding proteins have usually been classified according to their functional properties into several families, such as the actin monomer-binding protein profilin (Carlsson *et al*, 1977); actin nucleators, including Arp2/3 and Formin that initiate *de novo* branched and unbranched filament assembly, respectively (Chen *et al*, 2010; Dong *et al*, 2003; Machesky *et al*, 1994; Pizarro-Cerda *et al*, 2017); the heterodimeric capping proteins that terminate F-actin elongation (Isenberg *et al*, 1980); severing/depolymerization factors Cofilin and Gelsolin (Bamburg *et al*, 1980; Barrie *et al*, 2024; Tanaka *et al*, 2018; Yin & Stossel, 1979); filament binding proteins, such as tropomyosin that binds to the main groove of an actin filament and stabilizes the filament (von der Ecken *et al*, 2015; Yu & Ono, 2006); and cross-linking proteins that crosslink and stabilize multiple F-actin filaments together for cell movement and muscle contraction (Le *et al*, 2017; Ribeiro Ede *et al*, 2014). The accumulation of 3-dimensional structures of ABPs in complex with actin revealed that different ABPs share a limited number of actin-binding structural modules (Van Troys *et al*, 1999). Thus, identifying and characterizing new

59 actin-binding structural modules will provide direct hints of the actin target site and the functional
60 effect on the actin dynamics of ABPs that share the specific actin-binding module.

61 Given actin's essential roles in eukaryotes, many prokaryotic and viral pathogens co-opt a
62 variety of mechanisms that target the host actin cytoskeleton for effective pathogenesis (Aktories
63 *et al*, 2011; Bugalhao *et al*, 2015). The virulence factor BimA from *Burkholderia*
64 *pseudomallei* mimics host actin-polymerizing proteins Ena/VASP to nucleate, elongate, and
65 bundle filaments (Benanti *et al*, 2015). The *Vibrio parahaemolyticus* VopL consists of a VopL C-
66 terminal domain (VCD) and three WASP homology 2 (WH2) motifs and mimics the Arp2/3
67 complex and formin proteins to stimulate actin polymerization (Namgoong *et al*, 2011; Zahm *et*
68 *al*, 2013). The *Salmonella* invasion protein A (SipA) effector is an actin-binding protein that
69 enhances actin polymerization and promotes the uptake efficiency of the bacterium (McGhie *et al*,
70 2004).

71 The Gram-negative bacterium *Legionella pneumophila* is the causative agent of a
72 potentially fatal form of pneumonia in humans named Legionnaires' disease (Cunha *et al*, 2016;
73 Fraser *et al*, 1977; McDade *et al*, 1977; Mondino *et al*, 2020). Upon entry into human alveolar
74 macrophage cells, the facultative intracellular pathogen translocates more than 350 different
75 bacterial proteins, known as effectors (Burstein *et al*, 2009; Huang *et al*, 2011; Zhu *et al*, 2011).
76 These effector proteins subvert multiple conserved eukaryotic pathways, such as ubiquitination
77 (Price & Abu Kwaik, 2021; Tomaskovic *et al*, 2022), autophagy (Choy *et al*, 2012; Omotade &
78 Roy, 2020; Thomas *et al*, 2020; Wan *et al*, 2024), lipid metabolism (Hsu *et al*, 2012; Swart &
79 Hilbi, 2020; Toulabi *et al*, 2013), and the actin cytoskeleton (Franco *et al*, 2012; Prashar *et al*,
80 2018; Zhang *et al*, 2023) to aid the pathogen in establishing a *Legionella*-containing vacuole (LCV)

81 amenable to intracellular growth and proliferation (Gomez-Valero *et al*, 2019; Mondino *et al.*,
82 2020; Oliva *et al*, 2018).

83 Like other bacterial pathogens, *L. pneumophila* utilizes a cohort of virulent effectors to
84 modulate actin. Recent studies revealed that the VipA effector nucleates actin and disrupts the
85 Multi-Vesicular Bodies (MVB) pathway (Franco *et al.*, 2012) and the RavK effector cleaves actin
86 to abolish actin polymerization (Liu *et al*, 2017). In our recent screen for *L. pneumophila* effectors
87 that affect host F-actin dynamics, we identified several novel effector proteins that exhibited
88 various degrees of F-actin-associated phenotypes. Among these positive hits, Lpg1387, an effector
89 with no known function, showed strong colocalization with F-actin. In this study, we report the
90 identification of a novel actin-binding motif consisting of a long anti-parallel α-helical hairpin. We
91 further revealed the molecular mechanism of actin-binding by cryo-electron microscopy (cryoEM)
92 and presented evidence for developing a potential F-actin probe based on this novel actin-binding
93 motif. Moreover, using click chemistry, we confirmed that, in addition to the actin-binding motif,
94 Lpg1387 has a lysine fatty-acylate (KFA) catalytic domain specific for small GTPases. Hence, we
95 named this *L. pneumophila* effector Lfat1 (*Legionella F-actin-binding fatty-acyl-transferase 1*).

96 ## Results

97 **The *Legionella* effector Lfat1 directly interacts with F-actin via a coiled-coil domain**

98 To explore how the intracellular bacterial pathogen *Legionella pneumophila* modulates
99 host actin dynamics, we performed a screen to search for effectors that perturb host actin structures.
100 In this screen, we imaged F-actin structures with phalloidin staining in HeLa cells transfected with
101 an GFP-effectors library. In this screen, several effectors showed various degrees of F-actin-
102 associated phenotypes (Figure S1). Among the positive hits, MavH (Lpg2425) has recently been
103 shown to polymerize actin filaments in a membrane-dependent manner (Zhang *et al.*, 2023).
104 Another effector, Lfat1 (Lpg1387), exhibited nearly a complete colocalization with F-actin (Figure
105 S1).

106 To elucidate the molecular mechanism of how Lfat1 localizes to F-actin filaments, we first
107 analyzed the 3-D structure predicted by AlphaFold (Jumper *et al*, 2021). The structure revealed a
108 hammer-like structure for the full-length Lfat1 protein (Figure 1A). The head of the hammer is
109 formed by a globular NC domain (N and C-terminal globular domain), which is contributed by
110 both the N-terminal (residue 1-137, red) and the C-terminal lobes (residues 356-469 pink) of the
111 protein, while the handle of the hammer is formed by an elongated, anti-parallel, coiled-coil hairpin
112 (CC-domain), which contains the middle portion of the protein (residues 138- 355, cyan). To map
113 the region responsible for Lfat1 F-actin localization, we created constructs expressing the NC- and
114 CC-domains fused with an N-terminal GFP, respectively, and investigated their intracellular
115 localization by fluorescence microscopy. Interestingly, while the NC-domain showed a diffused
116 cytosolic localization, the CC-domain exhibited a high colocalization to actin filaments
117 comparable to the wild-type protein (Figure 1B and C). This result was further confirmed by an
118 immunoprecipitation (IP) experiment wherein full-length Lfat1 and the CC-domain were able to

119 pulldown actin whereas the NC-domain could not (Figure 1D). To test whether the CC-domain
120 directly binds actin, we performed an *in vitro* F-actin co-sedimentation assay, in which purified
121 recombinant proteins of the CC-domain were incubated with actin in the presence of G-actin or F-
122 actin buffer. Following ultracentrifugation to pellet F-actin, the supernatant and pellet were
123 analyzed on SDS-PAGE (Figure 1E). In the G-actin buffer, both actin and the CC-domain protein
124 remained in the supernatant; however, the CC-domain protein co-sedimented with the polymerized
125 F-actin in the F-actin buffer, indicating that the CC-domain of Lfat1 directly binds to F-actin.
126 Strikingly, when the CC-domain protein was incubated with actin at a 1:1, 1:2, or 1:4 (actin : CC)
127 molar ratio in the F-actin buffer, an approximately equal amount of CC-domain proteins were co-
128 sedimented with F-actin, and the excess CC-domain proteins remained in the supernatant. This
129 observation indicates that the interaction between the CC-domain and actin is saturable, and the
130 binding occurs at a one-to-one molar ratio (Figure 1F). Together, our findings identified Lfat1 as
131 a novel actin-binding effector of *Legionella*. We further demonstrated that Lfat1 binds F-actin at
132 a one-to-one stoichiometry through a unique, long coiled-coil hairpin CC-domain, which we will
133 henceforth call the actin-binding domain (ABD). .

134 **Cryo-EM structure of the Lfat1 ABD-F-actin complex**

135 The discovery of a novel ABD triggered us to interrogate the molecular mechanism of
136 actin-binding by this ABD. We sought to determine the cryo-electron microscopy (cryo-EM)
137 structure of the Lfat1 ABD-F-actin complex. In our initial attempts to prepare the protein complex,
138 F-actin bundles were readily induced by Lfat1 ABD with the F-actin buffer, making it hard to
139 solve a single F-actin filament for structural determination (data not shown). To restrict excessive
140 actin polymerization, equal molar of Lfat1 ABD and G-actin were incubated in a non-polymerizing
141 G-actin buffer overnight at 4°C. The protein complex sample was then applied to cryo-grids,

142 vitrified, and loaded to a 200kV Thermo Fisher Talos Arctica transmission electron microscope
143 for Cryo-EM data collection. The data were processed, and a high-resolution density map (average
144 to 3.5 angstroms resolution) was calculated and refined using CryoSPARC (Punjani *et al*, 2017).
145 The atomic model of the complex was built by docking the F-actin structure (PDB: 7BTI) and the
146 AlphaFold-predicted model of Lfat1 ABD into the CryoEM density using ChimeraX (Meng *et al*,
147 2023). The model was then refined iteratively using Phenix (Liebschner *et al*, 2019), and the final
148 model was validated online by wwPDB validation server at https://validate.wwpdb.org (Figure
149 S2 and Supplemental Table 1).

150 The CryoEM density map of the complex allowed a complete resolution of the actin
151 subunit in the F-actin filament, including its bound ADP and Mg^{2+} ion (Figure 2A, Figure S3A
152 and B). The D-loop (DNase I-binding loop) of the actin monomer adopts a closed conformation.
153 The D-loop of the nth actin monomer extends into the hydrophobic cleft between actin subdomains
154 1 and 3 of the $n+2^{nd}$ actin monomer. The hydrophobic residues (V45, M46, V47, and M49) at the
155 tip of the D-loop pack against a large hydrophobic area lining the wall of the hydrophobic cleft of
156 the $n+2^{nd}$ actin monomer (Figure 2B). The D-loop also mediates specific hydrogen bond
157 interactions between the two adjacent actin monomers. The main chain amino group of V47 and
158 the carbonyl group of K52 of the D-loop hydrogen bond with the hydroxyl groups of Y145 and
159 Y171, respectively (Figure 2B).

160 The cryo-EM structure also revealed the distal portion of the coiled-coil hairpin, which
161 consists of about 1/3 of the entire Lfat1 ABD domain (Figure S3D). The proximal end of the ABD
162 domain is not visible, likely due to its flexibility, and zeroed out in 2D-class averaging. The
163 structure revealed that the two α-helices of the Lfat1 ABD domain are zipped together by a stretch
164 of hydrophobic residues, mostly leucines and isoleucines (Figure 2C). The ABD domain radiates

165 away from the central F-actin core with its tip of the hairpin region binding to the site between two
166 adjacent actin molecules within each strand of the F-actin filament (Figure 2A). The ABD domain
167 embeds a surface area of 3703 $Å^2$ on the actin filament, which is contributed by both the D-loop
168 region of the nth and the hydrophobic cleft of the $n+2^{nd}$ actin monomers (Figure S4). Several
169 hydrophobic residues (Y240, L241, and L244) located at the tip of the ABD hairpin are
170 accommodated by a hydrophobic pocket formed between the two adjacent actin molecules (Figure
171 2D). The interaction between the ABD domain and the actin filament also involves several
172 hydrogen bonds. The hydroxyl group of Y240 of the ABD domain forms a hydrogen bond with
173 the main chain carbonyl group of V47 at the D-loop; the amino group of D248 of the ABD pairs
174 with the carbonyl oxygen of G48; and the side chain carbonyl oxygen of ABD Q254 makes
175 hydrogen bond with the main chain amine group of S352 of actin. Moreover, salt bridges are also
176 observed between R236 of the ABD domain and D27 and E336 of the $n+2^{nd}$ actin monomer (Figure
177 2D).

178 Together, our cryo-EM structure of the Lfat1 ABD domain in complex with F-actin
179 revealed the intricate molecular basis of multivalent interactions between F-actin and a novel
180 prokaryotic actin-binding domain. In addition, the complex structure revealed a 1:1 ratio of the
181 interaction between the Lfat1 ABD and actin monomer, which is in agreement with the
182 stoichiometry determined by the previous co-sedimentation experiment (Figure 2A, Figure S3C
183 and D).

184

185 **Validation of key residues on the ABD domain in its recognition of F-actin**

186 To validate our structural observations of the interaction between Lfat1 ABD and F-actin,
187 we performed an alanine substitution mutagenesis experiment of three representative residues
188 (R236, Y240, and Q254) in the Lfat1ABD domain (Figure 3A). We found that GFP-tagged R236A
189 or Q254A ABD mutant showed a slight increase in diffused signals, with the majority of proteins
190 remaining colocalized with F-actin. However, the Y240A mutation renders the protein mostly
191 cytosolic (Figures 3B and C). To further validate the fluorescence imaging results, we performed
192 an *in vitro* F-actin co-sedimentation titrating assay to measure the binding affinity between ABD
193 proteins and F-actin (Figure 3D and E). The apparent K_d for wild-type ABD to F-actin is calculated
194 at about 1.48 μM, which is on par with LifeAct (K_d of 2.2 μM) (Riedl *et al*, 2008). Consistently,
195 the K_d for R236A and Q254A mutants increased about 10-fold, 19.06 and 16.28 μM, respectively.
196 More strikingly, the Y240A mutant showed a substantial decrease in affinity with a K_d of 63.69
197 μM (Figure 3D and E). In summary, the mutagenesis experiments confirmed that multivalent
198 interactions contribute to the binding of Lfat1 ABD with F-actin with hydrophobic interactions
199 playing a central role, and the affinity and specificity were further enhanced by hydrogen bond
200 and salt bridge interactions.

201

202 **Comparison of Lfat1 ABD with other actin-binding domains**

203 The discovery of a novel ABD from the *Legionella* effector Lfat1 prompted us to compare
204 this unique ABD to other representative actin-binding proteins. Although ABDs adopt a diverse
205 structural fold, most of them share a similar interaction scheme with F-actin by targeting a hotspot
206 encompassing the D-Loop of $Actin_n$ and the hydrophobic cleft of $Actin_{n+2}$ (Figure 4A and B)
207 (Dominguez, 2004). For example, LifeAct, which is derived from the first 17 residues from
208 *Saccharomyces cerevisiae* ABP140 (Riedl *et al.*, 2008), utilizes the hydrophobic residues aligned

209 on one side of its amphipathic α-helix to engage primarily hydrophobic interactions with a small
210 hydrophobic patch at the F-actin hotspot (Belyy *et al*, 2020; Kumari *et al*, 2020). The actin-binding
211 CH1 domain of Utrophin (a neuromuscular junction scaffolding protein) contains multiple F-actin
212 binding sites (Keep, 2000; Keep *et al*, 1999). Two of the actin-binding sites on the CH1 domain
213 interact primarily with the D-loop region of the nth actin monomer, and the third one, consisting of
214 the N-terminal α-helix, spills the interface further into the subdomain I region of the nth actin
215 subunit (Kumari *et al.*, 2020). The *Pseudomonas aeruginosa* effector protein, Exotoxin Y or ExoY,
216 uses its C-terminal "anchor" helix to engage primarily hydrophobic interactions with the
217 hydrophobic cleft in subdomain 1 of the $n+2^{nd}$ actin subunit (Belyy *et al*, 2021) in a way similar
218 to that of LifeAct (Belyy *et al.*, 2020). ExoY also contains a peptide, which meanders on the
219 surface of the $n+2^{nd}$ actin subunit and functions as a "sensor" for the actin activator but contributes
220 little affinity to F-actin binding (Belyy *et al.*, 2021). These examples support that the hydrophobic
221 cleft formed by subdomain 1 and 3 is the "hotspot" for many ABDs, and the binding site on actin
222 is frequently extended to the vicinity of the "hotspot" depending on unique features associated
223 with each ABD (Figure 4A).

224 A structural comparison of the ABD-F-actin complex structures also revealed that the actin
225 D-loop adopts a variety of conformations upon the binding of different ABDs (Figure 4B). In
226 globular G-actin, the D-Loop is either disordered or adopts an α-helix, depending on its nucleotide
227 state or binding with G-actin binding proteins (Graceffa & Dominguez, 2003). In F-actin, the D-
228 Loop inserts itself into the hydrophobic target-binding cleft of the n+2 subunit immediately above
229 it (Das *et al*, 2020; Dominguez & Holmes, 2011). The D-loop region is also involved in direct
230 interactions with many ABDs (Figure 4). In the Lfat1 ABD and F-actin complex, specific
231 hydrogen bonds are formed between the backbone carbonyl group of D-loop residues V47 and

232 G48 and the ABD residues Y240 and D248 (Figure 2D). These hydrogen bonding interactions
233 cause the D-loop to insert slightly deeper into the hydrophobic cleft and induce a unique
234 conformation of the D-loop residues G50 and Q51 (*Bos taurus* numbering, equivalent to G48 and
235 Q49 in *G. gallus*) not observed in other structures (Figure 4B). This observation suggests that
236 although the hydrophobicity of the "hotspot" plays a dominant role in ABD-binding, the capacity
237 to accommodate the large variety of actin-binding motifs at the "hot spot" is likely due to the
238 structural plasticity of the D-loop.

239

240 **Engineering novel F-actin probes derived from the Lfat1 ABD**

241 Fluorescent toxins or proteins are frequently used as F-actin probes in fixed or live cells,
242 however, they all have certain limitations (Belin *et al*, 2014; Courtemanche *et al*, 2016; Lemieux
243 *et al*, 2014; Munsie *et al*, 2009). The discovery of a new F-actin binding domain from the
244 *Legionella* effector Lfat1 inspired us to investigate whether it can be developed as an alternative
245 *in vivo* F-actin probe. We first tried to map the minimum F-actin binding region in Lfat1 ABD. A
246 series of ABD truncations: ABD-S1 (residues 171-323), ABD-S2 (190-306), and ABD-S3 (211-
247 280) were created and transiently expressed in Hela cells. All three truncated versions
248 demonstrated specific colocalization with F-Actin comparable to the full-length ABD (Figure 5A).
249 However, further shortening of this ABD resulted in loss of function and exhibited a complete
250 cytosolic location (data not shown). Thus, our studies revealed a novel F-actin probe consisting of
251 a 70 amino acid-long alpha-helix hairpin.

252 The Lfat1 ABD contains two long alpha helixes forming a hairpin. We next asked whether
253 this ABD remains functional if the alpha-helix hairpin is split into two individual alpha helixes.

254 To test this, we fused an N-terminal mCherry with α1 and a C-terminal GFP with the α2 of the
255 ABD, respectively, and examined their intracellular localization. All these single alpha helix
256 fusions showed a diffused localization (Figure S5A, B), however, to our surprise, when the two
257 fusion constructs encoding full-length ABD-α1 and α2 were expressed together, these two alpha
258 helixes were able to form a functional ABD and colocalized with F-Actin as the intact wild type
259 ABD (Figure 5C and D). Interestingly, the alpha helixes derived from ABD-S1 could also
260 reconstitute a functional F-actin probe, but not the further shortened alpha helices derived from
261 ABD-S2 (Figures 5C and D). These results suggested that the F-actin probe derived from the Lfat1
262 ABD can be used in a split form, providing flexibility to this new probe.

263

264 **Lfat1 is a lysine fatty acyltransferase (KFAT)**

265 The AlphaFold-predicted structure of Lfat1 revealed a globular domain composed of the
266 N- and C-terminus beside the central, coiled-coil hairpin (Figure 1A). Structural homology search
267 using the DALI server (Holm & Rosenstrom, 2010) yielded the top hit as the RID (Rho GTPase
268 Inactivation Domain) toxin from the *Vibrio vulnificus* (PDB:5XN7) with a Z-score of 7.9. The
269 catalytic domain of both proteins contains a central β-sheet flanked by multiple α helices. The
270 conserved catalytic dyad (H38 and C403) in Lfat1 were positioned with a similar orientation to
271 the dyad in the RID toxin (H2595 and C2835) (Figure 6A).

272 The RID toxin is a lysine fatty acyltransferase (KFAT) processed from a much larger
273 prototoxin that transfers long acyl chains to the ε-amine of lysines in small GTPases, such as those
274 in the Rac subfamily (Zhou *et al*, 2017). To determine whether Lfat1 possesses a similar KFAT
275 activity, we probed the fatty acylation of a small GTPase Rac3. Briefly, HEK-293T cells were co-

276 transfected with plasmids expressing Flag-Rac3 and GFP-Lfat1 or its catalytic mutants followed
277 by treatment with Alk14, a clickable chemical analog of palmitic acid modified with a terminal
278 alkyne moiety. Flag-Rac3 proteins were enriched from transfected cells by immunoprecipitation
279 and were then conjugated to an azide-containing fluorophore, TAMRA-N_3 via copper-catalyzed
280 cycloaddition (Hein *et al*, 2008). The reaction products were separated by SDS-PAGE and
281 analyzed by in-gel fluorescence detection and Western blot. Robust fluorescence signals
282 associated with Rac3 were detected in the presence of wild-type Lfat1, but not its H38A or C403A
283 catalytic mutants (Figure 6B). Furthermore, we found that Rac3-associated fluorescence signals
284 were stable even after the hydroxylamine (HA) treatment, which can reverse acylation on cysteine
285 but not lysine residues. We next asked whether Lfat1 can fattyacylate other host targets. To address
286 this question, we performed a click chemistry-coupled SILAC (Stable Isotope Labeling by Amino
287 Acids in Cell Culture) mass-spectrometry experiment to identify potential targets (Figure S6A).
288 Interestingly, nearly half of the top hits are small GTPases, including Rabs, RheB, RalA, and
289 Rap1B (Figure S6B). Fattyacylation by Lfat1 on several of the small GTPases was further verified
290 using click chemistry (Figure S6C-F). Furthermore, the fatty acylation of small GTPases by Lfat1
291 does not appear to depend on F-actin binding, as these substrates were still modified by the actin-
292 binding-deficient Lfat1 Y240A mutant (Figures S7A and B). Together, our results demonstrated
293 that the *Legionella* effector Lfat1 is a *bona fide* KFAT that potentially fattyacylates host small
294 GTPases when exogenously expressed in cultured cells.

295 ## Discussion

296 In this study, we identified a novel actin-binding domain from *Leginella pneumophila*. This
297 prokaryote-originated ABD has an alpha-helical hairpin-like structure, which is unprecedented
298 from any other known ABDs. We further mapped the minimum region (~ 70 residues) required
299 for actin binding and demonstrated the feasibility of using this prokaryote ABD as an alternative
300 F-actin probe. Another unique and potentially useful characteristic of this probe is its ability to
301 function as a split-ABD. Although the individual alpha helix derived from the Lfat1 ABD fails to
302 bind actin, they were able to reconstitute a functional intact ABD when co-expressed. This unique
303 feature can be harnessed to target multi-component biological complexes to F-actin by genetically
304 fusing individual components to the split alpha helixes. Furthermore, our cryo-EM structure
305 revealed that the Lfat1 ABD intersects with F-actin obliquely. Its N- and C-termini are pointed
306 away with an adjustable distance from the filament depending on the size of the designed ABD.
307 Thus, the Lfat1 ABD can be used to target proteins of interest to F-actin with a tunable distance
308 from the filament to achieve spatial distribution-related specificity.

309 F-actin probes are essential tools in cell biology for visualizing and studying the dynamics
310 of the actin cytoskeleton in living and fixed cells. These probes come in various forms, including
311 fluorescently labeled phalloidins, actin-binding proteins, and genetically encoded fluorescent actin
312 markers (Melak *et al*, 2017). Each type of probe has its advantages and limitations. The choice of
313 probe depends on the specific experimental requirements, such as whether live-cell imaging is
314 needed, the level of perturbation that can be tolerated, and the ease of use. The toxic chemical
315 derived from fungi, phalloidin, has been developed as the gold standard F-actin marker to stain
316 actin in fixed samples and tissues (Cooper, 1987). However, it is not suitable for live-cell imaging
317 due to its toxicity and low cell permeability. Many yeast- or human-derived actin-binding domains

318 have been developed into F-actin probes by fusion with fluorescent proteins. Lifeact (Riedl *et al.*,
319 2008), utrophin (Burkel *et al*, 2007), and F-tractin (Brehm *et al*, 2004) are the three most
320 commonly used genetically encoded probes. Although these probes have been widely used for
321 live-cell imaging, they suffer from problems such as low affinity for F-actin and perturbation in
322 actin dynamics. Our discovery of a novel ABD offers an alternative F-actin probe that not only
323 can be used to study actin dynamics but also can be used to as a versatile anchor to target specific
324 activities to F-actin.

325 The discovery of Lfat1 as an F-actin–binding lysine fatty acyl transferase raised the
326 intriguing question of whether its enzymatic activity depends on F-actin binding. Recent studies
327 have shown that other *Legionella* effectors, such as LnaB and Ceg14, use actin as a co-factor to
328 regulate their activities. For instance, LnaB binds monomeric G-actin to enhance its phosphoryl-
329 AMPylase activity toward phosphorylated residues, resulting in unique ADPylation modifications
330 in host proteins (Fu *et al*, 2024; Wang *et al*, 2024). Similarly, Ceg14 is activated by host actin to
331 convert ATP and dATP into adenosine and deoxyadenosine monophosphate, thereby modulating
332 ATP levels in *L. pneumophila*–infected cells (He *et al*, 2025). However, this does not appear to be
333 the case for Lfat1. We found that Lfat1 mutants defective in F-actin binding retained the ability to
334 modify host small GTPases when expressed in cells (Figure S7). These findings suggest that, rather
335 than serving as a co-factor, F-actin may serve to localize Lfat1 via its actin-binding domain (ABD),
336 thereby confining its activity to regions enriched in F-actin and enabling spatial specificity in the
337 modification of host targets.

338 Our finding that Lfat1 is a protein lysine fatty acyl transferase provides important insights
339 to understand the physiolical function of Lfat1. The Rho Inactivation Domain (RID) is a module
340 found in Multifunctional-Autoprocessing Repeats-in-Toxin (MARTX) toxins produced by certain

341 Gram-negative pathogenic bacteria, such as *Vibrio cholerae* and *Vibrio vulnificus* (Satchell, 2015).
342 RID primarily targets the Rho GTPase family members by the covalent attachment of long-chain
343 fatty acids to the ε-amino groups of lysine residues. The modification inactivates the small
344 GTPases, leading to disruption of the actin cytoskeleton and consequent cell rounding and hence
345 facilitating bacterial invasion and impairing host immune responses (Zhou *et al.*, 2017). A recent
346 study reported that RID modifies other host proteins, notably septins. Fatty-acylation on septins
347 alters the localization and compromises the host cell structural integrity (Xu *et al*, 2024). In this
348 study, we demonstrated that the globular NC-domain of Lfat1 exhibits KFAT activity when
349 overexpressed *in vivo*. Using Click chemistry, we showed that Lfat1 could fatty-acylate lysines of
350 the host small GTPase Rac3 (Figure 6B) and other small GTPases (Figure S6). Many of the small
351 GTPase substrates we identified, are known to associate with and regulating actin. For example,
352 RhoG regulates the actin cytoskeleton in lymphocytes (Vigorito *et al*, 2003); Rap1 is reported to
353 regulate actin reorganization and microtuble organizing center polarization at the B cell immune
354 synapse (Wang *et al*, 2017); RheB is reported to regulate actin filament distribution (Gau *et al*,
355 2005); Ral GTPases (RalA and RalB) links Ras, Rac, Rho signaling to control cell migration (Zago
356 *et al*, 2019); and RAB8A regulates spindle migration via ROCK-mediated actin assembly in mouse
357 oocyte meiosis (Pan *et al*, 2019). The identification of the KFAT effectors among all *Legionella*
358 species and set up a solid foundation for further characterizations of this family of effectors.
359 However, future studies will be needed to identify which substrates are physiologicaly important
360 under infection conditions.

Acknowledgments

We thank Dr. Sheng Zhang and Dr. Qin Fu for helping with the proteomics study. W.Z. acknowledges support from the T32 training grant and the Sadov Graduate Student Fellowship (Cornell University). This work is supported by the National Institutes of Health R01GM144452(Y.M.), R01AI153110 (H.L.), and HHMI.

367 **Material and methods**

368 **Plasmid construction**

369 Please refer to Supplemental Table 2 for constructs used in this study. All targeted DNA
370 fragments were amplified by PCR using the primers listed in Supplemental Table 3. The amplified
371 DNA fragments were digested by restriction enzymes, BamHI and XhoI, and ligated to
372 corresponding vector plasmids. Plasmids containing the targeted genes were amplified using
373 NEB® Stable Competent C3040I *E. coli* strain and verified by sequencing. For mutagenesis,
374 plasmids containing wild-type genes were used as templates with mutagenic primers in a PrimeStar
375 MasterMix PCR reaction to amplify the entire plasmid, followed by DpnI digestion, and plasmids
376 carrying the desired mutations were amplified using the C3040I *E. coli* strain and verified by
377 sequencing.

378

379 **Protein purification**

380 Actin was purified from muscle acetone powder prepared from ground beef (Pardee &
381 Spudich, 1982). Briefly, 10 grams of muscle acetone powder was dissolved with 200 ml G-actin
382 buffer (5 mM Tris pH 7.5, 0.2 mM $CaCl_2$, 0.2 mM ATP, 0.5 mM DTT) at 4 ºC with stirring for 30
383 minutes followed by low-speed centrifugation at 5000-10,000g for 10-20 minutes to remove
384 insoluble solids. Soluble extracts were centrifuged at 15,000g for 60 min at 4 ºC, and actin was
385 precipitated by the slow addition of solid ammonium sulfate to reach 25% saturation. Precipitates
386 were collected by centrifugation at 15,000g for 30 min and dissolved in 50 ml G-actin buffer and
387 dialyzed against 2 liters of G-actin buffer overnight with two changes of buffer. The dialyzed actin
388 solution was centrifuged at 32,000g for 60 min to remove any aggregates. Actin was polymerized

389 by the addition of 10x polymerization buffer to a final solution containing 150 mM KCl, 2 mM
390 $MgCl_2$, 2 mM EGTA, and 1 mM ATP. Polymerization was allowed to proceed for 30 min at 25 °C,
391 then in a cold room for 90 min. F-actin was pelleted by centrifugating at 100,000g for 30 min, and
392 the pellet was resuspended in 10–20 ml G-actin buffer and homogenized in a glass-glass
393 homogenizer on ice. The suspension was dialyzed against 2 liters of G-actin buffer for 48 hours
394 with four changes of dialysis solution to completely depolymerize the F-actin. The solution was
395 further clarified by centrifugation at 32,000g for 60 min. The clarified supernatant was loaded onto
396 a Sephadex G-150 or Sephacryl S-100 HR column, equilibrated in G-actin buffer, to remove the
397 remaining contaminating G-actin-binding proteins. Peak fractions were analyzed by SDS- PAGE,
398 pooled, and flash-frozen in liquid nitrogen before storage.

399 Recombinant Lfat1 ABD (WT and mutants) proteins were expressed in Rosetta *E. coli*.
400 The expression was induced by 0.1 mM IPTG at 18 ºC overnight. The bacteria were harvested by
401 centrifugation at 4,000 RPM using the Beckman Coulter JLA-9.1000 rotor for 20 minutes. The
402 cell pellets were lysed in Buffer A (20 mM Tris pH7.5, 150 mM NaCl) using sonication. The
403 whole cell lysate was then centrifuged at 16,000 RPM using the Beckman Coulter JA-25.50 rotor
404 for 40 minutes at 4 ºC, and the clarified lysate was then bound to Cobalt resins on a rotator at 4 ºC
405 for 2 hours. The resins were then extensively washed with Buffer A, and the ABD proteins were
406 released from the resin by a SUMO-specific protease, Ulp1. The released proteins were collected
407 and further purified using size-exclusion chromatography on a Superdex S75 column. The purified
408 ABD proteins were concentrated and then flash-frozen in liquid nitrogen for storage.

409

410 **Cell culture and co-immunoprecipitation**

411 HEK293T and HeLa cells were maintained at a low passage and grown in DMEM
412 (Dulbecco's Modified Eagle Medium) supplemented with 10% FBS (fetal bovine sera). For
413 transfection, plasmids were mixed with 1 mg/ml PEI (polyethylenimine MW10K, Millipore Sigma)
414 at a 5:1 ratio in DMEM incubated for 15 minutes at room temperature, and added directly to cells.
415 After 24 hours of transfection, the cells were used either for immunoprecipitation or imaging
416 experiments.

417 For immunoprecipitation, HEK293T cells transfected with the indicated plasmids after 24
418 hours were chilled on ice, washed with ice-cold PBS, and detached using lysis buffer (20 mM Tris
419 pH7.5, 150 mM NaCl, 1 mM DTT, 0.5% Triton X-100, 0.1% sodium deoxycholate, 1 mM PMSF,
420 with Roche protease inhibitor cocktail). The cells were then lysed using a sonicator on ice. The
421 lysate was clarified by centrifugation at 16,000 RPM using the Beckman Coulter JA-25.50 rotor
422 for 15 minutes at 4 ºC. The lysate was then incubated with anti-GFP nanobody beads for 2 hours
423 with rotating. The mixture was then washed in a buffer containing 20 mM Tris pH7.5, 150 mM
424 NaCl, 1 mM DTT, and 0.5% Triton X-100. The washed beads were then dissolved in 1X SDS
425 loading buffer, and the samples were analyzed by SDS-PAGE followed by Western-blot and
426 scanned using Li-COR Odyssey CLx scanner.

427

428 **Fluorescence Microscopy**

429 HeLa cells grown on glass cover slides were transfected with the indicated plasmids after
430 24 hours. The cells were then washed with PBS and fixed in 4% PFA in PBS for 15 minutes at
431 room temperature. The fixed cells were washed twice with PBS and incubated with Odyssey
432 blocking buffer with 0.1% saponin and rhodamine- or CF647-phalloidin (Thermofisher) for 1 hour

433 at room temperature. The stained cells were washed three times with PBS and mounted on a glass
434 specimen slide with Fluoromount-G (Thermofisher), and were imaged using a 3i spinning-disc
435 confocal fluorescence microscope. Line-scan analysis was performed using ImageJ (Schneider *et*
436 *al*, 2012).

437

438 **CryoEM sample preparation, data collection, data processing**

439 Purified G-actin (1 mg/ml) was mixed with an equal molar of ABD in G-actin buffer and
440 incubated overnight at 4 ºC. The ABD-F-actin complex samples with a serial dilution were applied
441 to a glow-discharged copper Quantifoil r1.2/1.3 grids and rapidly plunged frozen in liquid ethane
442 using FEI-Vitrobot-Mark-IV. The vitrified grids were then transferred to liquid nitrogen for
443 storage and data collection.

444 For data collection, the grids were imaged using a ThermoFisher Talos Arctica 200 kV
445 electron microscope with a K3 direct electron detector and a Gatan bioquantum energy filter and
446 the dataset was collected using SerialEM software using the following parameters: -0.4 to -3.0 µm
447 defocus range, pixel size of 1.5879062 Å, total electron dose of 40.68 electrons per $Å^2$, exposure
448 time of 1.23 seconds, 50 frames per movie, and 4548 total movies. The movies were then imported
449 into CryoSPARC (Punjani *et al.*, 2017) for motion correction and patch-CTF estimation. 2173 out
450 of 4548 micrographs were selected after manual curation. The CryoSPARC Helical Tracer job
451 was utilized to perform particle picking with a minimum particle diameter of 50 Å and a maximum
452 diameter of 100 Å, with each particle separated by 100 Å. A total of 1,733,108 particles were
453 extracted from micrographs using a box size of 480 pixels. Iterative 2D classifications were
454 performed on these particles, and low-resolution classes were discarded after each iteration.

455 Finally, 1,220,462 particles were used for ab-initio initial model building, followed by iterative
456 helical and local refinements. Final map was sharpened using CryoSPARC's Sharpening Tool
457 using half maps and a B-factor of 58.87 as obtained from the Guinier plot.

458

459 **Model building, refinement, validation**

460 The atomic model of F-actin (PDB: 7BTI) and the AlphaFold-predicted model of
461 Lfat1ABD were docked into the finalized CryoEM density using ChimeraX 1.25 (Pettersen *et al*,
462 2021). The atomic model of the F-actin-ABD complex was then refined iteratively using Phenix
463 (Adams *et al*, 2010), and the final model, CryoEM full-map and half-maps, were validated by the
464 Worldwide Protein Data Bank (wwPDB).

465

466 **F-actin co-sedimentation assay**

467 Recombinant Lfat1 ABD was mixed with buffer control or G-actin at a final concentration
468 of 20 μM. The mixed samples were either incubated in G-actin buffer or F-actin polymerization
469 buffer (50 mM KCl, 2 mM MgCl2) at room temperature for 30 minutes followed by centrifugation
470 at 70,000 RPM using the Beckman Coulter TLA-100.3 rotor for 30 minutes at 4 ºC. The
471 supernatant and pellet were then analyzed on SDS-PAGE.

472 To determine the F-actin binding affinity of ABD, purified recombinant Lfat1 ABD WT
473 and mutant proteins were diluted in G-actin buffer in a series of concentration at 0, 1.25, 2.5, 5,
474 7.5, 10, 15, 20, 30, 40, 50, 60 μM and were incubated with 20 μM of G-actin. Actin polymerization
475 was initiated at room temperature for 30 minutes by adding F-actin polymerization buffer. The

476 samples were then centrifugated at 70,000 RPM using the Beckman Coulter TLA-100.3 rotor for
477 30 minutes at 4 ºC, and the supernatants and pellets were then analyzed on SDS-PAGE and staining
478 Coomas Brilliant Blue dye, and the intensity of the bands was quantified using ImageJ. and the
479 intensity of the ABD band was divided by the intensity of the actin band in the pellet fractions to
480 calculate the % of ABD bound to F-actin. The average of each data point from three independent
481 experiments was then plotted, and an exponential fit was used to calculate the apparent K_d in R
482 studio.

483

484 **Protein fatty-acylation detection via Click chemistry**

485 Indicated plasmids were transfected into HEK 293T cells using PEI transfection reagent.
486 After overnight transfection, cells were treated with 50 μM Alk14 (Cayman Chemical) for 6 hours.
487 The cells were washed with ice-cold PBS and then lysed in lysis buffer (25 mM Tris-HCl, pH 7.8,
488 150 mM NaCl, 10% glycerol, and 1% NP-40) with protease inhibitor cocktail at 4 °C for 30 min.
489 After centrifugation at 17,000 g for 30 min at 4 ºC, the supernatant was collected and incubated
490 with 20 μL of anti-Flag affinity beads (Sigma Aldrich) at 4 °C for 2 h. The affinity beads was
491 washed three times with washing buffer (25 mM Tris-HCl, pH 7.8, 150 mM NaCl, 0.2% NP-40)
492 and resuspended in 20 μL of washing buffer. TAMRA-N3 (Lumiprobe), TBTA (TCI chemicals),
493 $CuSO_4$, and TCEP (Millipore) were added into the reaction mixture in the order listed. The click
494 chemistry reaction was allowed to proceed at room temperature for 30 min. The reaction was
495 quenched by adding 6x SDS loading dye and boiled for 5 min. Where indicated, samples were
496 treated with hydroxylamine (HA) to remove cysteine fatty acylation. The samples were then
497 separated on SDS-PAGE and fixed in a buffer (50% CH_3OH, 40% water and 10% acetic acid) by

498 shaking for 1 hours at 4ºC and then washed and store in water. The gel was scanned to record
499 fluorescence signal using a ChemiDoc MP (BioRad).

500

501 **SILAC sample preparation and MS data analysis**

502 SILAC samples were prepared from cells transiently expressing WT or H38A mutant Lfat1
503 using a published protocol (Kosciuk *et al*, 2020). The samples were then trypsin digested and the
504 peptides were analyzed using an Orbitrap Fusion™ Tribrid™ (Thermo-Fisher Scientific) mass
505 spectrometer. The MS and MS/MS spectra were subjected to database searches using Proteome
506 Discoverer (PD) 2.4 software (Thermo Fisher Scientific, Bremen, Germany) with the Sequest HT
507 algorithm. The database search was conducted against a *Homo sapiens* Uniprot database with the
508 following variable modifications: methionine oxidation; deamidation of asparagine/glutamine;
509 SILAC heavy: R10 (10.008 Da) and K8 (8.014 Da) and light labeling on R and K; palmitoylation
510 plus biotin on K, protein N-terminus and fixed modification of cysteine carbamidomethylation.

511

512 **References**

513

514 Adams PD, Afonine PV, Bunkoczi G, Chen VB, Davis IW, Echols N, Headd JJ, Hung LW, Kapral GJ, Grosse-
515 Kunstleve RW *et al* (2010) PHENIX: a comprehensive Python-based system for macromolecular
516 structure solution. *Acta Crystallogr D Biol Crystallogr* 66: 213-221
517 Aktories K, Lang AE, Schwan C, Mannherz HG (2011) Actin as target for modification by bacterial protein
518 toxins. *FEBS J* 278: 4526-4543
519 Bamburg JR, Harris HE, Weeds AG (1980) Partial purification and characterization of an actin
520 depolymerizing factor from brain. *FEBS Lett* 121: 178-182
521 Barrie KR, Rebowski G, Dominguez R (2024) Mechanism of actin filament severing and capping by gelsolin.
522 *Nat Struct Mol Biol*
523 Belin BJ, Goins LM, Mullins RD (2014) Comparative analysis of tools for live cell imaging of actin network
524 architecture. *Bioarchitecture* 4: 189-202
525 Belyy A, Merino F, Mechold U, Raunser S (2021) Mechanism of actin-dependent activation of nucleotidyl
526 cyclase toxins from bacterial human pathogens. *Nat Commun* 12: 6628
527 Belyy A, Merino F, Sitsel O, Raunser S (2020) Structure of the Lifeact-F-actin complex. *PLoS Biol* 18:
528 e3000925
529 Benanti EL, Nguyen CM, Welch MD (2015) Virulent Burkholderia species mimic host actin polymerases to
530 drive actin-based motility. *Cell* 161: 348-360
531 Brehm MA, Schreiber I, Bertsch U, Wegner A, Mayr GW (2004) Identification of the actin-binding domain
532 of Ins(1,4,5)P3 3-kinase isoform B (IP3K-B). *Biochem J* 382: 353-362
533 Bugalhao JN, Mota LJ, Franco IS (2015) Bacterial nucleators: actin' on actin. *Pathog Dis* 73: ftv078
534 Burkel BM, von Dassow G, Bement WM (2007) Versatile fluorescent probes for actin filaments based on
535 the actin-binding domain of utrophin. *Cell Motil Cytoskeleton* 64: 822-832
536 Burstein D, Zusman T, Degtyar E, Viner R, Segal G, Pupko T (2009) Genome-scale identification of
537 Legionella pneumophila effectors using a machine learning approach. *PLoS Pathog* 5: e1000508
538 Carlsson L, Nystrom LE, Sundkvist I, Markey F, Lindberg U (1977) Actin polymerizability is influenced by
539 profilin, a low molecular weight protein in non-muscle cells. *J Mol Biol* 115: 465-483
540 Chen Z, Borek D, Padrick SB, Gomez TS, Metlagel Z, Ismail AM, Umetani J, Billadeau DD, Otwinowski Z,
541 Rosen MK (2010) Structure and control of the actin regulatory WAVE complex. *Nature* 468: 533-538
542 Choy A, Dancourt J, Mugo B, O'Connor TJ, Isberg RR, Melia TJ, Roy CR (2012) The Legionella effector RavZ
543 inhibits host autophagy through irreversible Atg8 deconjugation. *Science* 338: 1072-1076
544 Cooper JA (1987) Effects of cytochalasin and phalloidin on actin. *J Cell Biol* 105: 1473-1478
545 Courtemanche N, Pollard TD, Chen Q (2016) Avoiding artefacts when counting polymerized actin in live
546 cells with LifeAct fused to fluorescent proteins. *Nat Cell Biol* 18: 676-683
547 Cunha BA, Burillo A, Bouza E (2016) Legionnaires' disease. *Lancet* 387: 376-385
548 Das S, Ge P, Oztug Durer ZA, Grintsevich EE, Zhou ZH, Reisler E (2020) D-loop Dynamics and Near-Atomic-
549 Resolution Cryo-EM Structure of Phalloidin-Bound F-Actin. *Structure* 28: 586-593 e583
550 Dominguez R (2004) Actin-binding proteins--a unifying hypothesis. *Trends Biochem Sci* 29: 572-578
551 Dominguez R, Holmes KC (2011) Actin structure and function. *Annu Rev Biophys* 40: 169-186
552 Dong Y, Pruyne D, Bretscher A (2003) Formin-dependent actin assembly is regulated by distinct modes of
553 Rho signaling in yeast. *J Cell Biol* 161: 1081-1092
554 Franco IS, Shohdy N, Shuman HA (2012) The Legionella pneumophila effector VipA is an actin nucleator
555 that alters host cell organelle trafficking. *PLoS Pathog* 8: e1002546
556 Fraser DW, Tsai TR, Orenstein W, Parkin WE, Beecham HJ, Sharrar RG, Harris J, Mallison GF, Martin SM,
557 McDade JE *et al* (1977) Legionnaires' disease: description of an epidemic of pneumonia. *N Engl J Med*
558 297: 1189-1197

559 Fu J, Li S, Guan H, Li C, Zhao YB, Chen TT, Xian W, Zhang Z, Liu Y, Guan Q *et al* (2024) Legionella maintains
560 host cell ubiquitin homeostasis by effectors with unique catalytic mechanisms. *Nat Commun* 15: 5953
561 Gau CL, Kato-Stankiewicz J, Jiang C, Miyamoto S, Guo L, Tamanoi F (2005) Farnesyltransferase inhibitors
562 reverse altered growth and distribution of actin filaments in Tsc-deficient cells via inhibition of both
563 rapamycin-sensitive and -insensitive pathways. *Mol Cancer Ther* 4: 918-926
564 Gomez-Valero L, Rusniok C, Carson D, Mondino S, Perez-Cobas AE, Rolando M, Pasricha S, Reuter S,
565 Demirtas J, Crumbach J *et al* (2019) More than 18,000 effectors in the Legionella genus genome
566 provide multiple, independent combinations for replication in human cells. *Proc Natl Acad Sci U S A*
567 116: 2265-2273
568 Graceffa P, Dominguez R (2003) Crystal structure of monomeric actin in the ATP state. Structural basis of
569 nucleotide-dependent actin dynamics. *J Biol Chem* 278: 34172-34180
570 He C, Li C, Liu Y, Chen TT, Li C, Chu X, Liu S, Wang L, Zhang Y, Ouyang S *et al* (2025) Modulation of host ATP
571 levels by secreted bacterial effectors. *Nat Commun* 16: 4675
572 Hein CD, Liu XM, Wang D (2008) Click chemistry, a powerful tool for pharmaceutical sciences. *Pharm Res*
573 25: 2216-2230
574 Holm L, Rosenstrom P (2010) Dali server: conservation mapping in 3D. *Nucleic Acids Res* 38: W545-549
575 Hsu F, Zhu W, Brennan L, Tao L, Luo ZQ, Mao Y (2012) Structural basis for substrate recognition by a unique
576 Legionella phosphoinositide phosphatase. *Proc Natl Acad Sci U S A* 109: 13567-13572
577 Huang L, Boyd D, Amyot WM, Hempstead AD, Luo ZQ, O'Connor TJ, Chen C, Machner M, Montminy T,
578 Isberg RR (2011) The E Block motif is associated with Legionella pneumophila translocated substrates.
579 *Cell Microbiol* 13: 227-245
580 Isenberg G, Aebi U, Pollard TD (1980) An actin-binding protein from Acanthamoeba regulates actin
581 filament polymerization and interactions. *Nature* 288: 455-459
582 Jumper J, Evans R, Pritzel A, Green T, Figurnov M, Ronneberger O, Tunyasuvunakool K, Bates R, Zidek A,
583 Potapenko A *et al* (2021) Highly accurate protein structure prediction with AlphaFold. *Nature* 596:
584 583-589
585 Keep NH (2000) Structural comparison of actin binding in utrophin and dystrophin. *Neurol Sci* 21: S929-
586 937
587 Keep NH, Winder SJ, Moores CA, Walke S, Norwood FL, Kendrick-Jones J (1999) Crystal structure of the
588 actin-binding region of utrophin reveals a head-to-tail dimer. *Structure* 7: 1539-1546
589 Kosciuk T, Price IR, Zhang X, Zhu C, Johnson KN, Zhang S, Halaby SL, Komaniecki GP, Yang M, DeHart CJ *et*
590 *al* (2020) NMT1 and NMT2 are lysine myristoyltransferases regulating the ARF6 GTPase cycle. *Nat*
591 *Commun* 11: 1067
592 Kumari A, Kesarwani S, Javoor MG, Vinothkumar KR, Sirajuddin M (2020) Structural insights into actin
593 filament recognition by commonly used cellular actin markers. *EMBO J* 39: e104006
594 Le S, Hu X, Yao M, Chen H, Yu M, Xu X, Nakazawa N, Margadant FM, Sheetz MP, Yan J (2017)
595 Mechanotransmission and Mechanosensing of Human alpha-Actinin 1. *Cell Rep* 21: 2714-2723
596 Lemieux MG, Janzen D, Hwang R, Roldan J, Jarchum I, Knecht DA (2014) Visualization of the actin
597 cytoskeleton: different F-actin-binding probes tell different stories. *Cytoskeleton (Hoboken)* 71: 157-
598 169
599 Letort G, Ennomani H, Gressin L, Thery M, Blanchoin L (2015) Dynamic reorganization of the actin
600 cytoskeleton. *F1000Res* 4
601 Liebschner D, Afonine PV, Baker ML, Bunkoczi G, Chen VB, Croll TI, Hintze B, Hung LW, Jain S, McCoy AJ *et*
602 *al* (2019) Macromolecular structure determination using X-rays, neutrons and electrons: recent
603 developments in Phenix. *Acta Crystallogr D Struct Biol* 75: 861-877
604 Liu Y, Zhu W, Tan Y, Nakayasu ES, Staiger CJ, Luo ZQ (2017) A Legionella Effector Disrupts Host Cytoskeletal
605 Structure by Cleaving Actin. *PLoS Pathog* 13: e1006186

606 Machesky LM, Atkinson SJ, Ampe C, Vandekerckhove J, Pollard TD (1994) Purification of a cortical complex
607 containing two unconventional actins from Acanthamoeba by affinity chromatography on profilin-
608 agarose. *J Cell Biol* 127: 107-115
609 McDade JE, Shepard CC, Fraser DW, Tsai TR, Redus MA, Dowdle WR (1977) Legionnaires' disease: isolation
610 of a bacterium and demonstration of its role in other respiratory disease. *N Engl J Med* 297: 1197-
611 1203
612 McGhie EJ, Hayward RD, Koronakis V (2004) Control of actin turnover by a salmonella invasion protein.
613 *Mol Cell* 13: 497-510
614 Melak M, Plessner M, Grosse R (2017) Actin visualization at a glance. *J Cell Sci* 130: 525-530
615 Meng EC, Goddard TD, Pettersen EF, Couch GS, Pearson ZJ, Morris JH, Ferrin TE (2023) UCSF ChimeraX:
616 Tools for structure building and analysis. *Protein Sci* 32: e4792
617 Mondino S, Schmidt S, Rolando M, Escoll P, Gomez-Valero L, Buchrieser C (2020) Legionnaires' Disease:
618 State of the Art Knowledge of Pathogenesis Mechanisms of Legionella. *Annu Rev Pathol* 15: 439-466
619 Munsie LN, Caron N, Desmond CR, Truant R (2009) Lifeact cannot visualize some forms of stress-induced
620 twisted F-actin. *Nat Methods* 6: 317
621 Namgoong S, Boczkowska M, Glista MJ, Winkelman JD, Rebowski G, Kovar DR, Dominguez R (2011)
622 Mechanism of actin filament nucleation by Vibrio VopL and implications for tandem W domain
623 nucleation. *Nat Struct Mol Biol* 18: 1060-1067
624 Oliva G, Sahr T, Buchrieser C (2018) The Life Cycle of L. pneumophila: Cellular Differentiation Is Linked to
625 Virulence and Metabolism. *Front Cell Infect Microbiol* 8: 3
626 Omotade TO, Roy CR (2020) Legionella pneumophila Excludes Autophagy Adaptors from the Ubiquitin-
627 Labeled Vacuole in Which It Resides. *Infect Immun* 88
628 Pan ZN, Lu Y, Tang F, Pan MH, Wan X, Lan M, Zhang Y, Sun SC (2019) RAB8A GTPase regulates spindle
629 migration and Golgi apparatus distribution via ROCK-mediated actin assembly in mouse oocyte
630 meiosisdagger. *Biol Reprod* 100: 711-720
631 Pardee JD, Spudich JA (1982) Purification of muscle actin. *Methods Enzymol* 85 Pt B: 164-181
632 Pettersen EF, Goddard TD, Huang CC, Meng EC, Couch GS, Croll TI, Morris JH, Ferrin TE (2021) UCSF
633 ChimeraX: Structure visualization for researchers, educators, and developers. *Protein Sci* 30: 70-82
634 Pizarro-Cerda J, Chorev DS, Geiger B, Cossart P (2017) The Diverse Family of Arp2/3 Complexes. *Trends*
635 *Cell Biol* 27: 93-100
636 Pollard TD (2016) Actin and Actin-Binding Proteins. *Cold Spring Harb Perspect Biol* 8
637 Prashar A, Ortiz ME, Lucarelli S, Barker E, Tabatabeiyazdi Z, Shamoun F, Raju D, Antonescu C, Guyard C,
638 Terebiznik MR (2018) Small Rho GTPases and the Effector VipA Mediate the Invasion of Epithelial Cells
639 by Filamentous Legionella pneumophila. *Front Cell Infect Microbiol* 8: 133
640 Price CTD, Abu Kwaik Y (2021) Evolution and Adaptation of Legionella pneumophila to Manipulate the
641 Ubiquitination Machinery of Its Amoebae and Mammalian Hosts. *Biomolecules* 11
642 Punjani A, Rubinstein JL, Fleet DJ, Brubaker MA (2017) cryoSPARC: algorithms for rapid unsupervised cryo-
643 EM structure determination. *Nat Methods* 14: 290-296
644 Ribeiro Ede A, Jr., Pinotsis N, Ghisleni A, Salmazo A, Konarev PV, Kostan J, Sjoblom B, Schreiner C,
645 Polyansky AA, Gkougkoulia EA *et al* (2014) The structure and regulation of human muscle alpha-actinin.
646 *Cell* 159: 1447-1460
647 Riedl J, Crevenna AH, Kessenbrock K, Yu JH, Neukirchen D, Bista M, Bradke F, Jenne D, Holak TA, Werb Z
648 *et al* (2008) Lifeact: a versatile marker to visualize F-actin. *Nat Methods* 5: 605-607
649 Satchell KJF (2015) Multifunctional-autoprocessing repeats-in-toxin (MARTX) Toxins of Vibrios. *Microbiol*
650 *Spectr* 3
651 Schneider CA, Rasband WS, Eliceiri KW (2012) NIH Image to ImageJ: 25 years of image analysis. *Nat*
652 *Methods* 9: 671-675

653 Swart AL, Hilbi H (2020) Phosphoinositides and the Fate of Legionella in Phagocytes. *Front Immunol* 11:
654 25
655 Tanaka K, Takeda S, Mitsuoka K, Oda T, Kimura-Sakiyama C, Maeda Y, Narita A (2018) Structural basis for
656 cofilin binding and actin filament disassembly. *Nat Commun* 9: 1860
657 Thomas DR, Newton P, Lau N, Newton HJ (2020) Interfering with Autophagy: The Opposing Strategies
658 Deployed by Legionella pneumophila and Coxiella burnetii Effector Proteins. *Front Cell Infect Microbiol*
659 10: 599762
660 Tomaskovic I, Gonzalez A, Dikic I (2022) Ubiquitin and Legionella: From bench to bedside. *Semin Cell Dev*
661 *Biol* 132: 230-241
662 Toulabi L, Wu X, Cheng Y, Mao Y (2013) Identification and structural characterization of a Legionella
663 phosphoinositide phosphatase. *J Biol Chem* 288: 24518-24527
664 Van Troys M, Vandekerckhove J, Ampe C (1999) Structural modules in actin-binding proteins: towards a
665 new classification. *Biochim Biophys Acta* 1448: 323-348
666 Vigorito E, Billadeu DD, Savoy D, McAdam S, Doody G, Fort P, Turner M (2003) RhoG regulates gene
667 expression and the actin cytoskeleton in lymphocytes. *Oncogene* 22: 330-342
668 von der Ecken J, Muller M, Lehman W, Manstein DJ, Penczek PA, Raunser S (2015) Structure of the F-actin-
669 tropomyosin complex. *Nature* 519: 114-117
670 Wan M, Minelli ME, Zhao Q, Marshall S, Yu H, Smolka M, Mao Y (2024) Phosphoribosyl modification of
671 poly-ubiquitin chains at the Legionella-containing vacuole prohibiting autophagy adaptor recognition.
672 *Nat Commun* 15: 7481
673 Wang JC, Lee JY, Christian S, Dang-Lawson M, Pritchard C, Freeman SA, Gold MR (2017) The Rap1-cofilin-
674 1 pathway coordinates actin reorganization and MTOC polarization at the B cell immune synapse. *J*
675 *Cell Sci* 130: 1094-1109
676 Wang T, Song X, Tan J, Xian W, Zhou X, Yu M, Wang X, Xu Y, Wu T, Yuan K *et al* (2024) Legionella effector
677 LnaB is a phosphoryl-AMPylase that impairs phosphosignalling. *Nature* 631: 393-401
678 Xu Y, Ding K, Peng T (2024) Chemical Proteomics Reveals N(epsilon)-Fatty-Acylation of Septins by Rho
679 Inactivation Domain (RID) of the Vibrio MARTX Toxin to Alter Septin Localization and Organization.
680 *Mol Cell Proteomics* 23: 100730
681 Yin HL, Stossel TP (1979) Control of cytoplasmic actin gel-sol transformation by gelsolin, a calcium-
682 dependent regulatory protein. *Nature* 281: 583-586
683 Yu R, Ono S (2006) Dual roles of tropomyosin as an F-actin stabilizer and a regulator of muscle contraction
684 in Caenorhabditis elegans body wall muscle. *Cell Motil Cytoskeleton* 63: 659-672
685 Zago G, Biondini M, Camonis J, Parrini MC (2019) A family affair: A Ral-exocyst-centered network links Ras,
686 Rac, Rho signaling to control cell migration. *Small GTPases* 10: 323-330
687 Zahm JA, Padrick SB, Chen Z, Pak CW, Yunus AA, Henry L, Tomchick DR, Chen Z, Rosen MK (2013) The
688 bacterial effector VopL organizes actin into filament-like structures. *Cell* 155: 423-434
689 Zhang Q, Wan M, Mao Y (2023) Membrane-dependent actin polymerization mediated by the Legionella
690 pneumophila effector protein MavH. *bioRxiv*
691 Zhou Y, Huang C, Yin L, Wan M, Wang X, Li L, Liu Y, Wang Z, Fu P, Zhang N *et al* (2017) N(epsilon)-Fatty
692 acylation of Rho GTPases by a MARTX toxin effector. *Science* 358: 528-531
693 Zhu W, Banga S, Tan Y, Zheng C, Stephenson R, Gately J, Luo ZQ (2011) Comprehensive identification of
694 protein substrates of the Dot/Icm type IV transporter of Legionella pneumophila. *PLoS One* 6: e17638

695

696 **Figure legends**

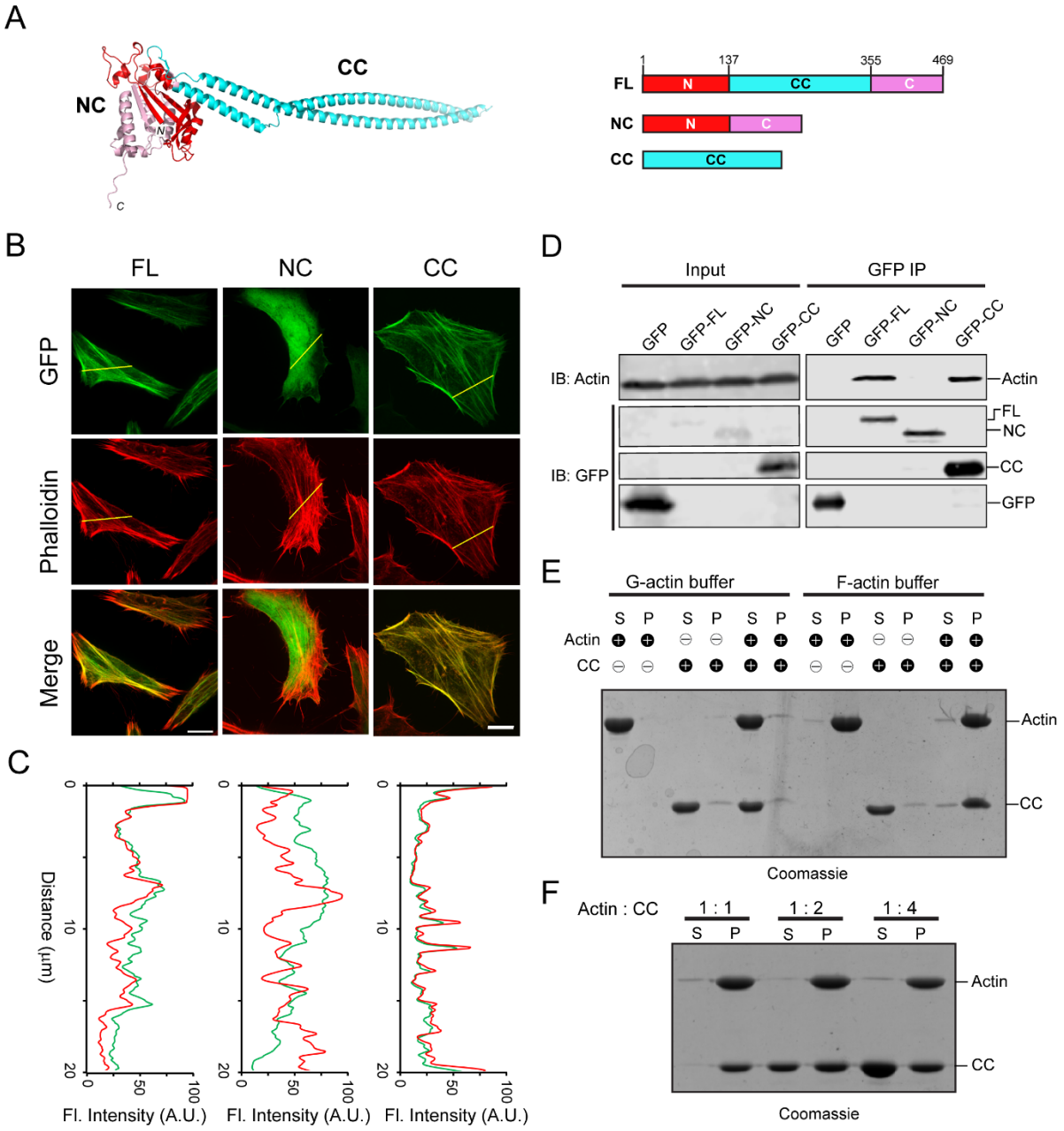

697

698 **Figure 1. Identification of LFat1 (lpg1387) as an F-actin binding effector**. (A) AlphaFold-
699 prediction structure of Lfat1 (Left) and domain architecture of Lfat1 (Right) with the N-terminal
700 domain shown in red, the C-terminal domain in pink, and the central coiled-coil domain in cyan.
701 FL: Full-length, NC: N and C globular domain, CC: Coiled-coil domain, respectively. (B) Cellular
702 localization of Lfat1-FL, -NC, or -CC as determined by fluorescence microscopy. HeLa cells

703 transiently expressing GFP-fused Lfat1-FL, -NC, or -CC were fixed and stained with phalloidin.
704 Scale bar = 10 μm. (C) Colocalization was determined by fluorescence intensity line scan along
705 the yellow line shown in (B). Red = F-actin, Green = GFP. (D) Co-immunoprecipitation to
706 determine interaction of Lfat1 with actin. HEK293T cells transiently expressing either GFP-empty
707 vector, -Lfat1 FL, -Lfat1 NC, or -Lfat1 CC were lysed, and cell lysates were immunoprecipitated
708 using anti-GFP nanobeads. The IP samples were analyzed with SDS-PAGE followed by
709 immunoblot against GFP and actin. (E) Co-sedimentation assay to determine direct interaction
710 between Lfat1 CC with F-actin. Purified G-actin, CC, or G-actin plus CC was incubated either in
711 G-actin buffer or F-actin polymerization buffer, then ultra-centrifuged to separate supernatant from
712 pellet, followed by analysis via SDS-PAGE. S: supernatant, P: pellet. (F) Binding stoichiometry
713 between Lfat1 CC and actin as determined by co-sedimentation assay.
714
715

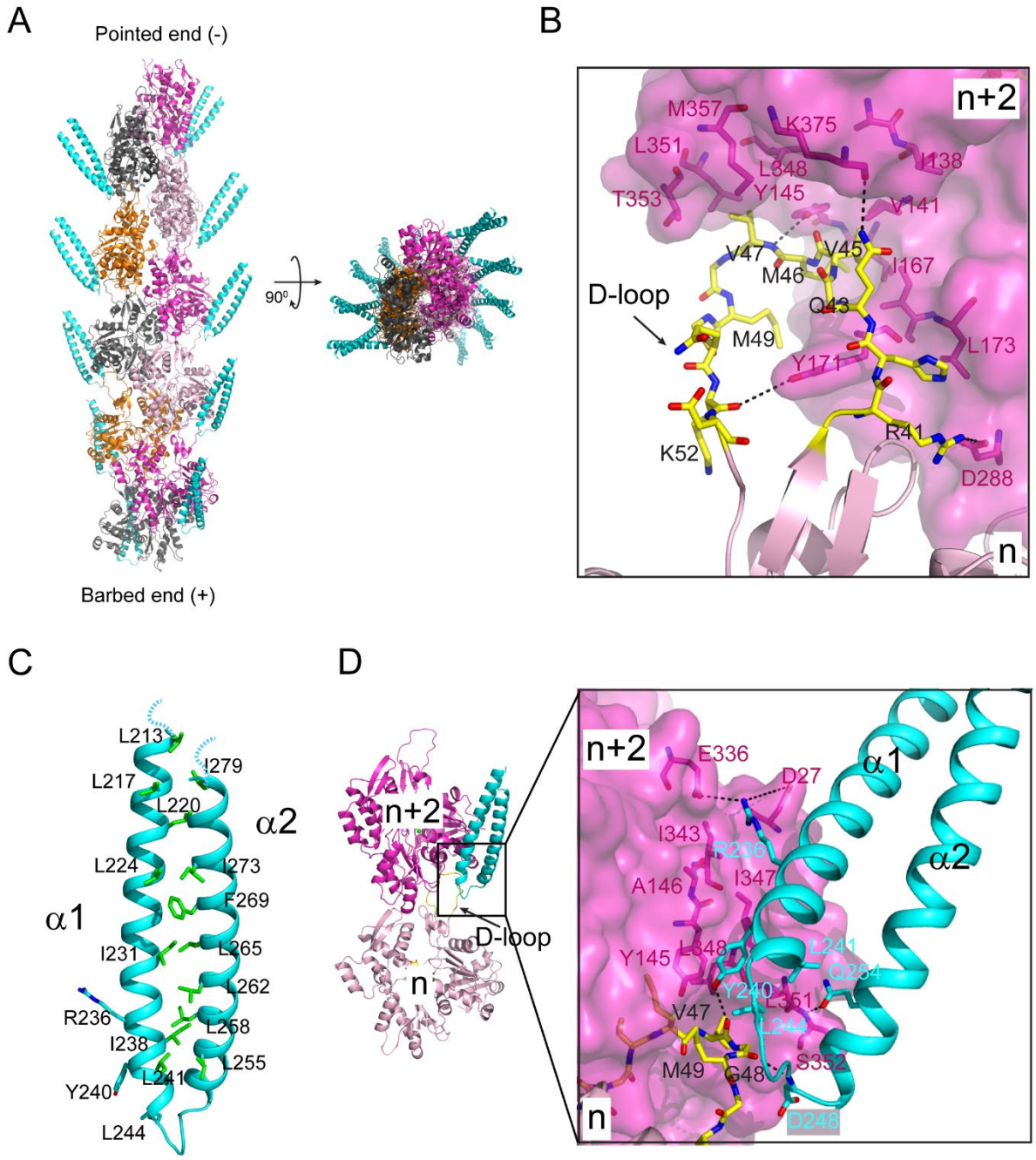

Figure 2. Cryo-EM structure of the Lfat1 ABD in complex with F-actin. (A) Cryo-EM structure of the F-actin-Lfat1 ABD complex. Left: side view of the structure positioned with the pointed end (-) up and barbed end (+) down. The visible part of ABD is colored in cyan. Right: Top view of the complex. (B) The D-loop conformation and its interactions in the hydrophobic cleft of the n+2nd actin monomer. (C) Ribbon diagram of the distal portion of the Lfat1 coiled-coil

722 domain. The two α-helices are zipped together through extensive hydrophobic interactions
723 contributed mainly by leucine and iso-leucine residues (shown in sticks). (D) Structural
724 representation of the interaction between the ABD domain of Lfat1 and F-actin. Inset: Extensive
725 hydrophobic, hydrogen bonding, and electrostatic interactions were observed between the Lfat1
726 ABD domain and the two adjacent actin monomers (details see in the text).
727

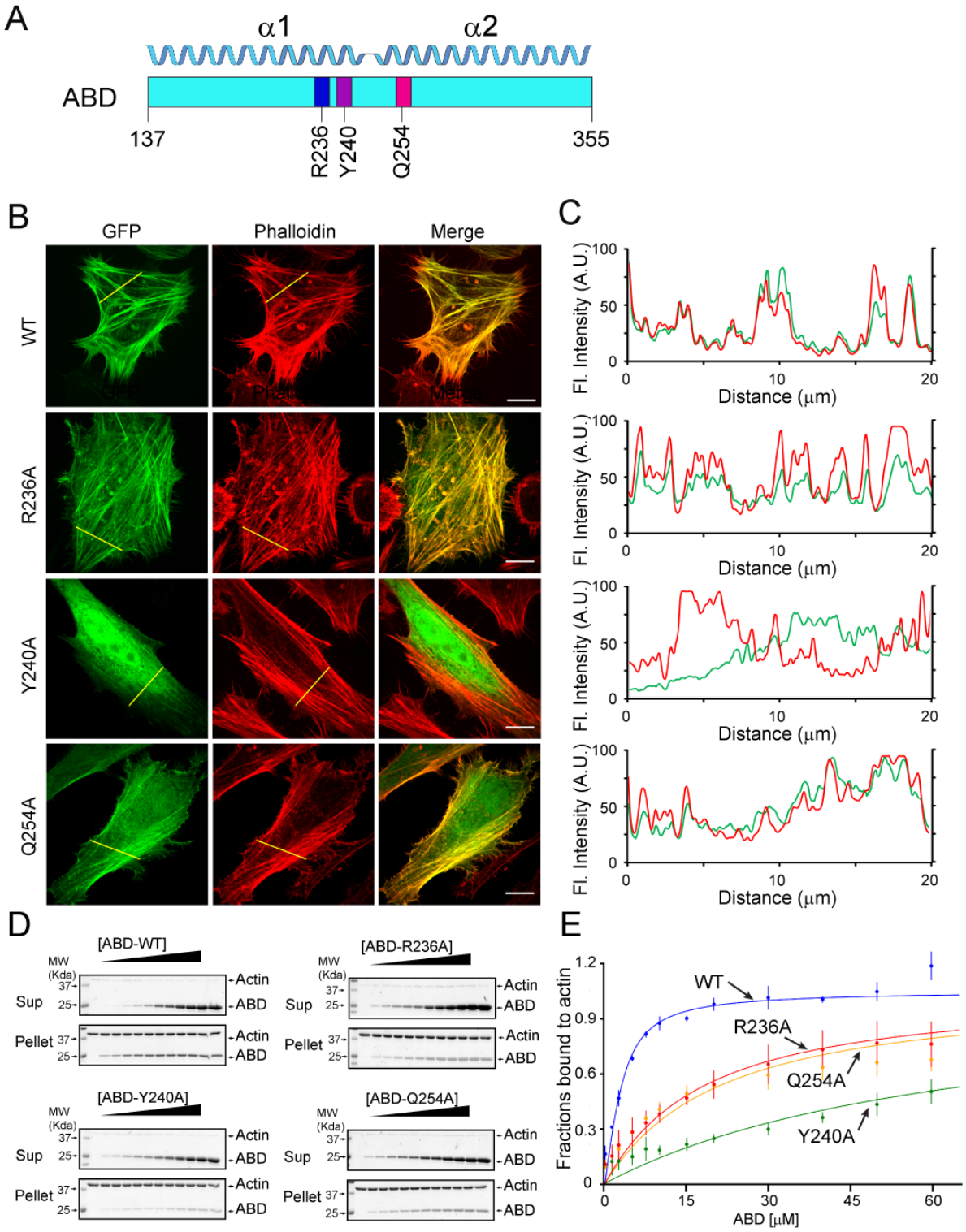

Figure 3. Validation of key Lfat1 ABD residues in their contributions to F-actin interactions.. (A) Schematic diagram of the Lfat1 ABD domain. Three key residues (R236, Y240, and Q254) involved in actin binding are labeled. (B and C) F-actin localization analysis of indicated ABD

732 mutants. GFP-Lfat1 WT, R236A, Y240A, or Q254A mutant was transiently expressed in HeLa
733 cells followed by fixation and staining with phalloidin. Fluorescence images were taken by a
734 confocal microscope and analyzed using Line scan along the indicated yellow lines. Scale bar =
735 10 μm. (D) Co-sedimentation assay of F-actin with WT and mutant Lfat1 ABD. Increasing
736 amounts (0 to 60 μM) of recombinant WT or mutant ABD proteins were incubated with a fixed
737 amount of actin. The samples were ultra-centrifugated after 30 min of room temperature incubation
738 in 1x actin polymerization buffer. The supernatant and pellet fractions were analyzed by SDS-
739 PAGE. (E) Quantitative analysis of the co-sedimentation titration data. The data point for each
740 concentration was averaged from three independent experiments. The error bar represents the
741 standard deviation.
742

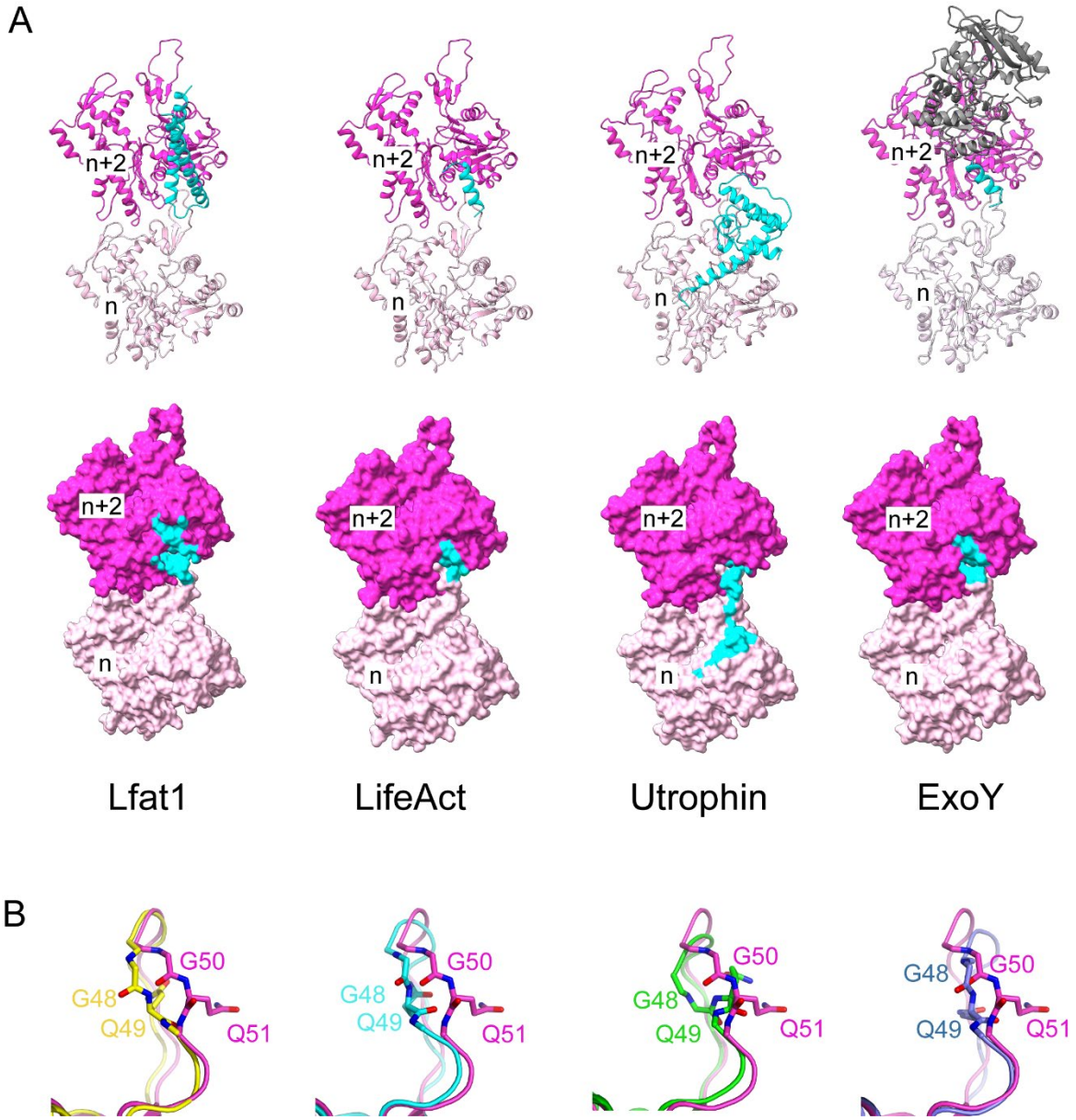

743

744 **Figure 4. Structural comparison between Lfat1 and other ABD-F-actin complexes.** (A)
745 Ribbon diagram (Upper row) and surface representation (bottom row) of two adjacent actin
746 monomers (purple and pink) bound with Lfat1 ABD, LifeAct (PDB ID: 7BTE), Utrophin (6M5G),
747 and ExoY (7P1G). The region interfacing with each ABD is colored in cyan. (B) Structural
748 comparison of the D-loop conformation in the Lfat1 ABD-F-actin complex (purple) with the D-
749 loop in other F-actin-ABD complexes. F-actin alone (yellow), LifeAct (cyan), Utrophin (green),

750 and ExoY (navy blue). Two D-loop residues with the largest deviation of backbone dihedral angles

751 (G50 and Q51) are shown in sticks.

752

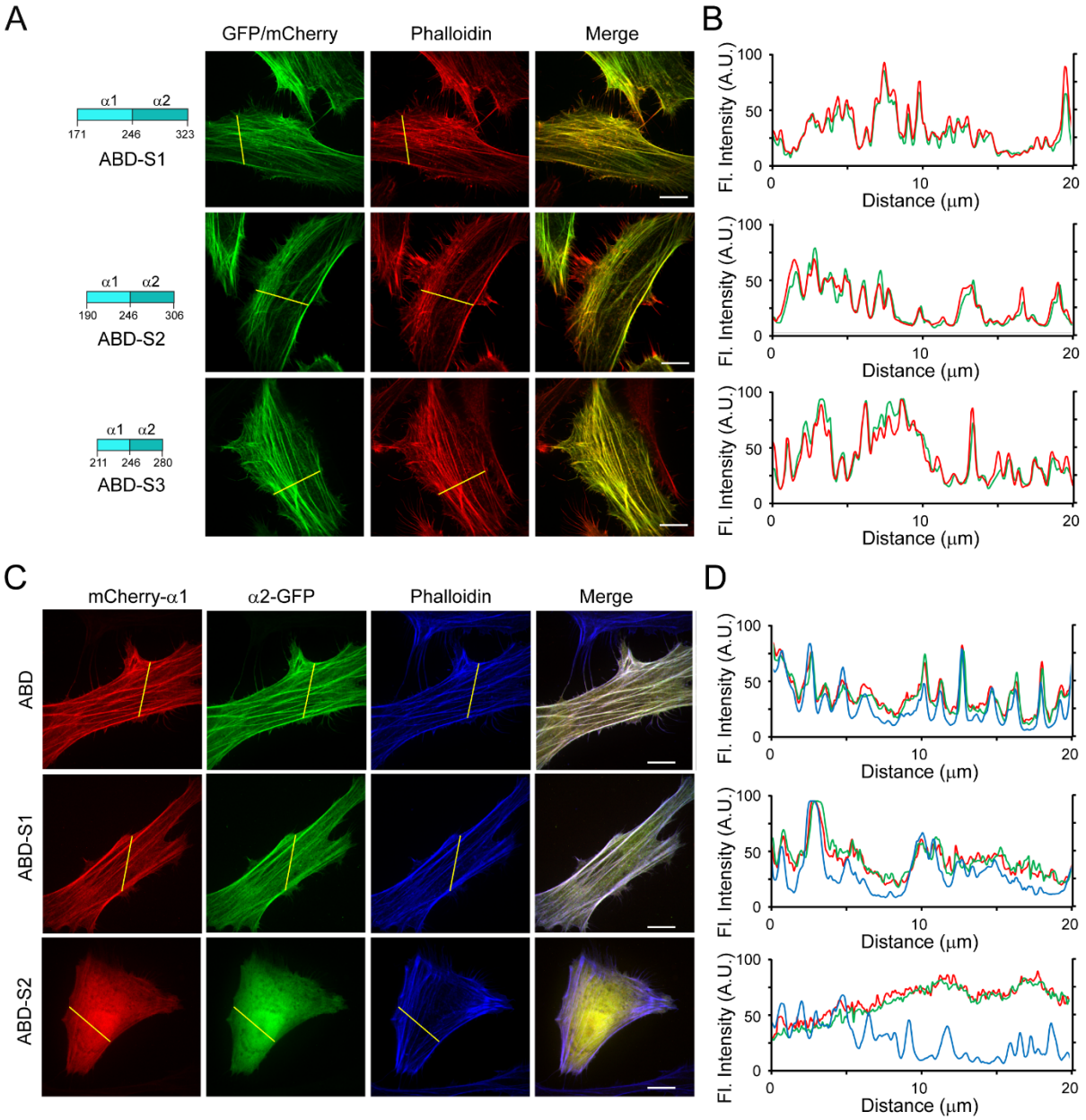

753

754 **Figure 5. Engineering Lfat1 ABD as an *in vivo* F-actin probe. (**A) Mapping the minimal actin-
755 binding domain of Lfat1. Schematic of shortened Lfat1ABD fragments used for F-actin binding
756 (Left). Representative fluorescence images of cells expressing indicated ABD fragments and
757 stained with rhodamine-phalloidin. (B) Line-scan analysis for the indicated ABD probes along the
758 yellow lines. (C) Representative fluorescence images of cells transiently transfected with plasmids
759 expressing separated alpha helixes (mCherry-α1 and α2-GFP) of ABD, ABD-S1, and ABD-S2.

760 The cells were fixed and stained with CF647-phalloidin. (D) Line-scan analysis of the images

761 shown in (C). Scale bar = 10 μm.

762

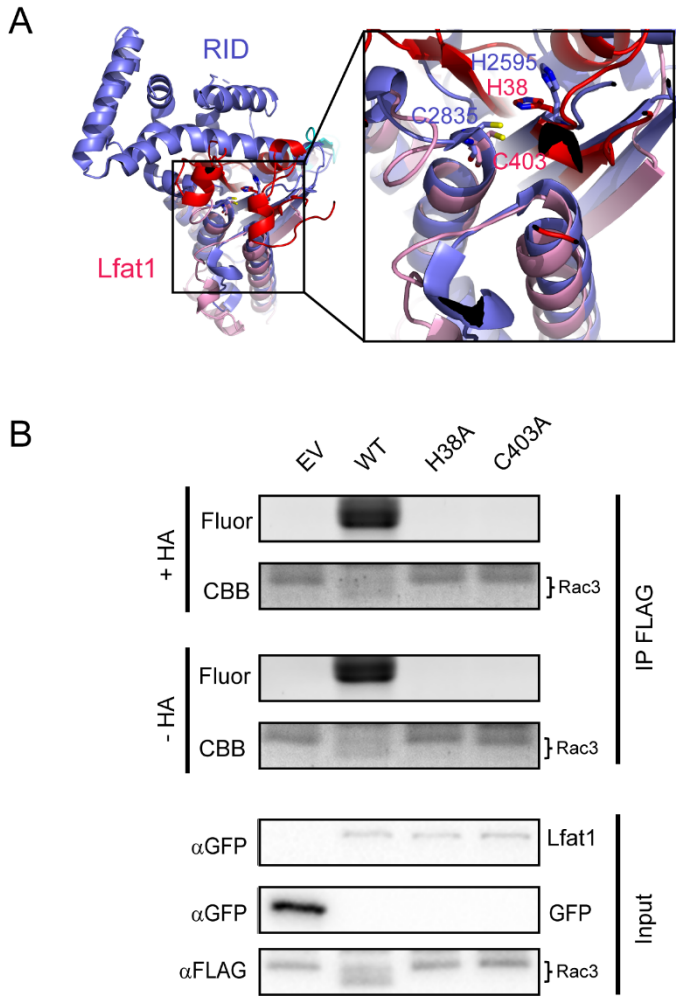

763

764 **Figure 6. Lfat1 is a lysine fatty acyltransferase that modifies eukaryotic small GTPases.** (A)
765 Ribbon representation of the *Vibrio vulnificus* RID (PDB ID: 5XN7) catalytic domain (purple)
766 superimposed with the AlphaFold-predicted NC-domain of Lfat1 (N-terminal domain in red, C-
767 terminal domain in pink). Inset: the catalytic pockets of the two proteins with conservation of the
768 catalytic histidine and cysteine between RID and Lfat1 shown in sticks. (B) Lfat1 catalyzes lysine
769 fatty acylation of Rac3. N-terminal Flag-tagged Rac3 was co-expressed with either GFP empty
770 vector (EV), GFP-Lfat1 WT, H38A, or C403A mutant in HEK293T cells for 24 hours. Flag-Rac3
771 was enriched using immunoprecipitation and subjected to Click chemistry. The samples were then
772 separated on SDS-PAGE and scanned for fluorescence signals.

773

774

775 **Table 1. CryoEM Data collection, refinement and validation statistics.**

Microscope	FEI Talos Artica
Voltage (keV)	200
Defocus range (um)	-0.4 to -3.0
Camera	K3 direct electron detector
Pixel size (Å)	0.833 (super-resolution)
Total electron dose (e/Å2)	40.68
Exposure time (seconds)	1.23
Frames per movie	50
Number of images	4548
3-D refinement statistics and helical symmetry	
Total number of particles	1,220,462
Resolution (Å)	3.58
Helical twist	-167
Rise	28
Model composition and validation	
Non-hydrogen atoms	34,740
Protein residues	4390
Ligands	10Mg, 10ADP
RMSD	
Bond lengths(Å)	0.25
Bond angles (°)	0.5
B-factor (Å2) Protein	58.87
B-factor (Å2) Ligand (ADP)	56.6
MolProbity Score	1.9
Clashscore	5
Ramachandran plot:-Favored	95
Allowed	5
Outlier	0
PDB ID	8VAA
EMDB Code	43087

776

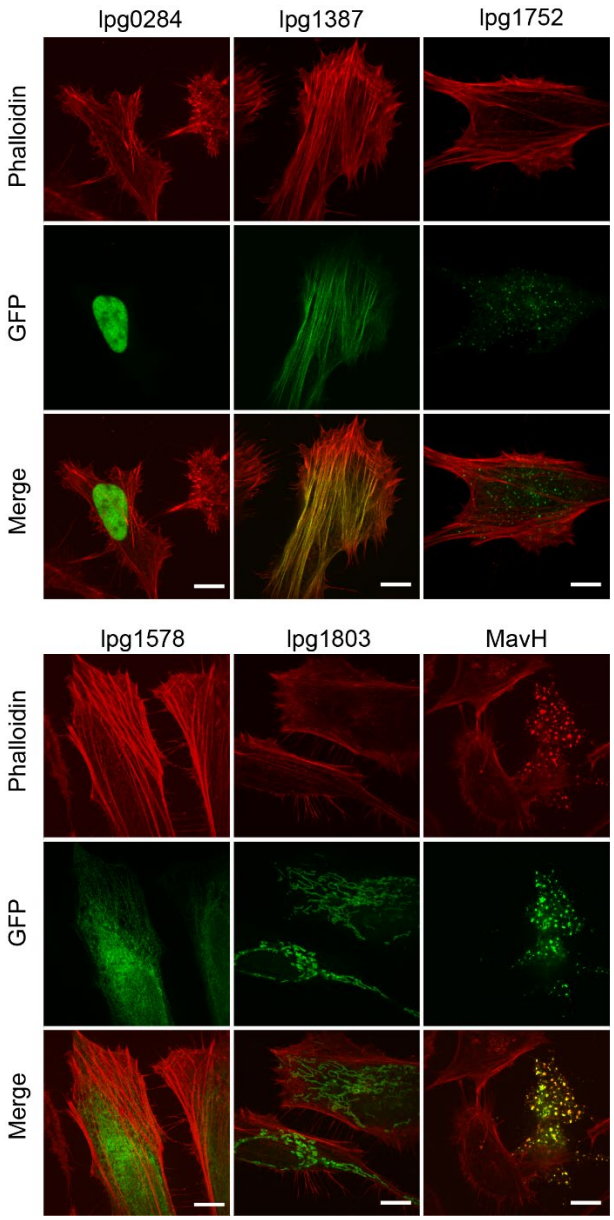

Figure 1 - Figure supplement 1. Intracellular localization representative Legionella effectors. Individual plasmid from a library consisting of 315 GFP-tagged *Legionella pneumophila* effectors was transiently expressed in HeLa cells followed by PFA fixation, stained with rhodamine-phalloidin, and visualized by fluorescence microscopy. Images showing intracellular localization of several representative effectors: lpg0284 (nuclear); lpg1387 and MavH (F-actin); lpg1578 (ER); and lpg1803 (mitochondrial). Scale bar = 10 μm.

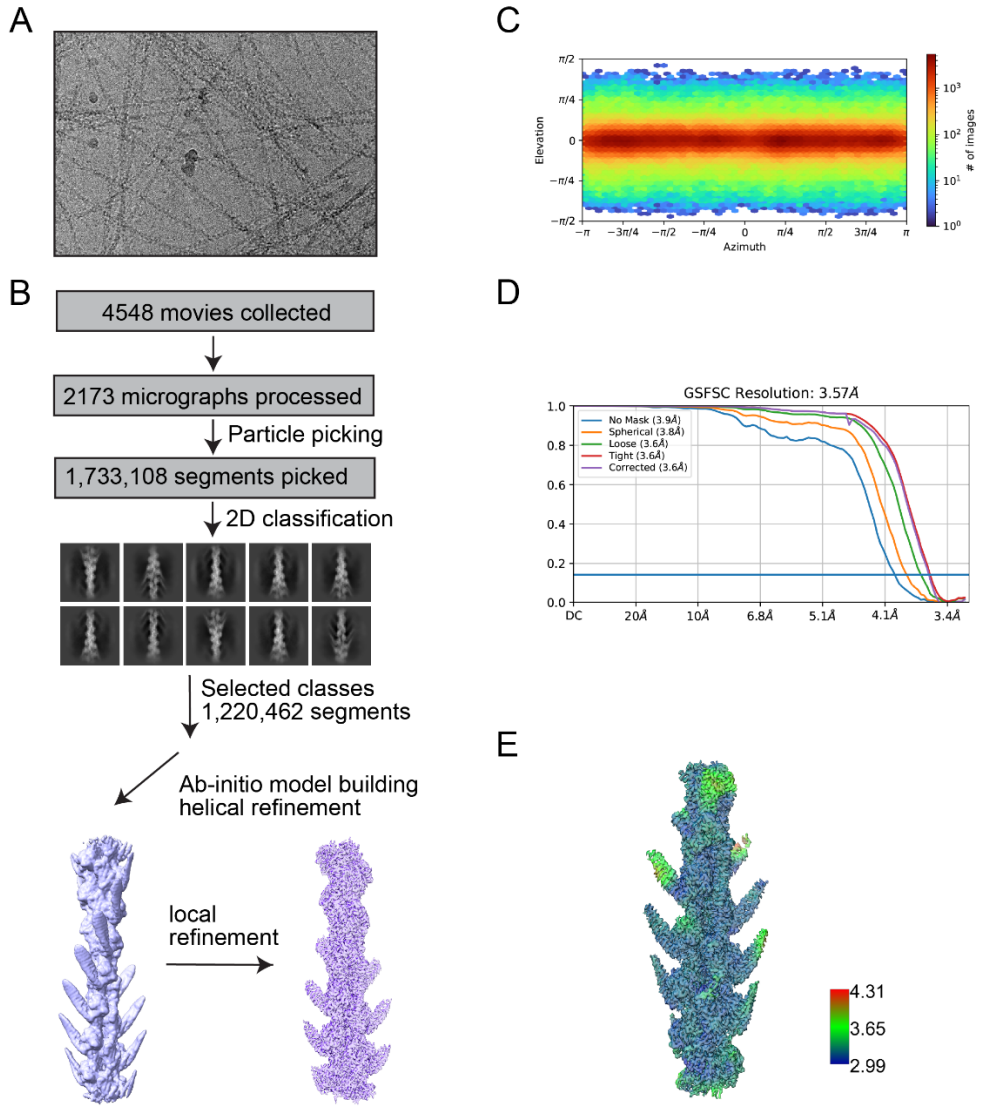

Figure 2 - Figure supplement 1. CryoEM data processing details of F-actin-Lfat1ABD complex. (A) Representative CryoEM micrograph of Lfat1ABD-F-actin complex. (B) Data-processing and structure determination workflow. Movies were collected at Talos Arctica electron microscope. Motion correction and patch CTF estimation were performed using CryoSPARC. Following manual curation, automatic filament tracer-based particle picking, and extraction, 1.2 million particles were 2-D classified and an ab initio model was built and refined using helical refinement until convergence. (C) Angular distribution of particles. (D) Resolution estimation by GSFSC. (E) Local resolution map of the final CryoEM map.

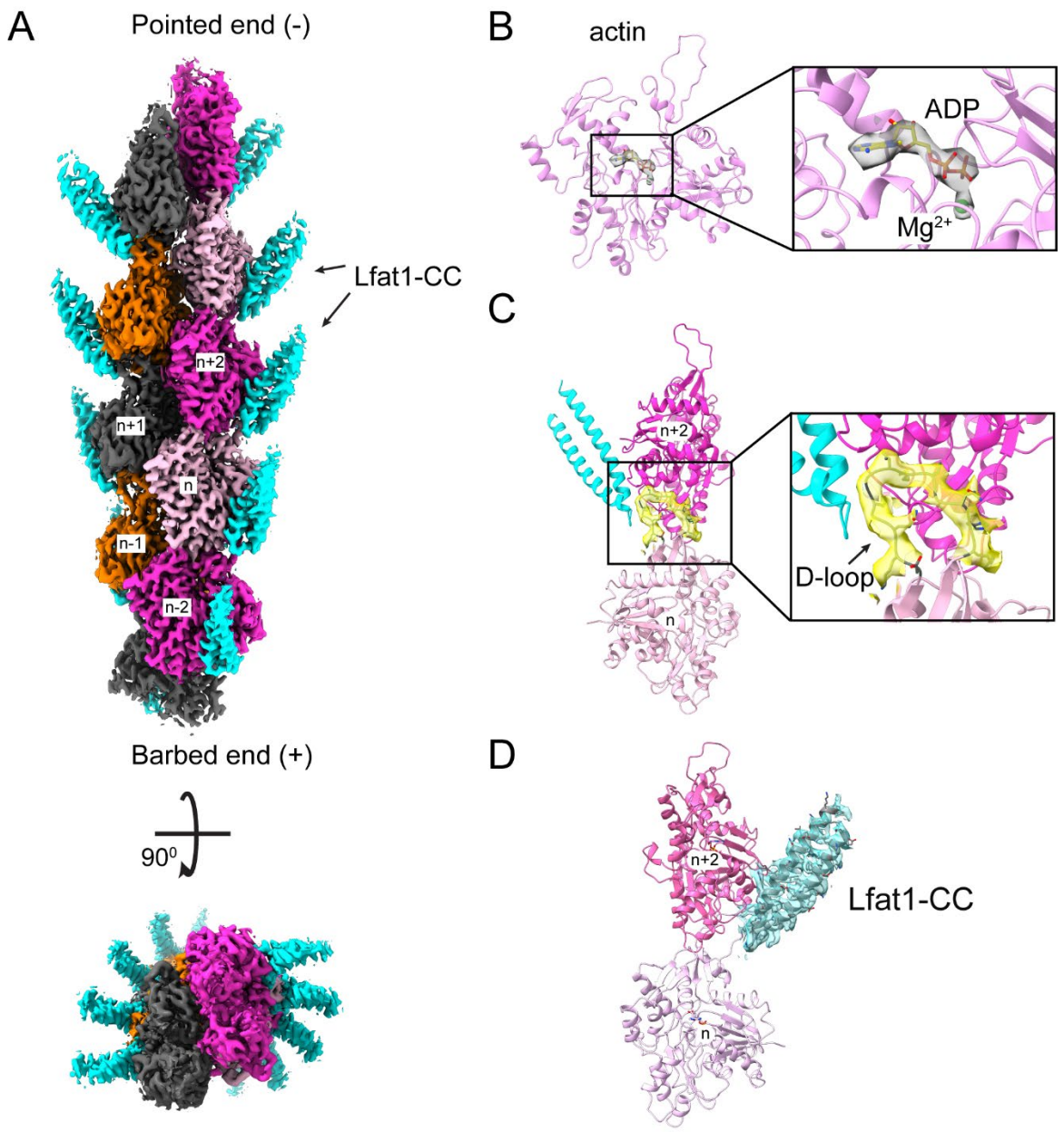

Figure 2 - Figure supplement 2. CryoEM maps of the F-actin-Lfat1ABD complex. (A) Final CryoEM density map of the complex. Top: Side view of the complex density map with the pointed end (-) up and barbed end (+) down. Lfat1 ABD is shown in cyan. Bottom: Top view of the complex density map. (B) The EM density map (grey) of ADP-Mg^{2+} at the ATP binding cleft of actin subunits. (C) The EM-map of actin D-loop (yellow). (D) The EM density map (cyan) of the distal region of the Lfat1 hairpin.

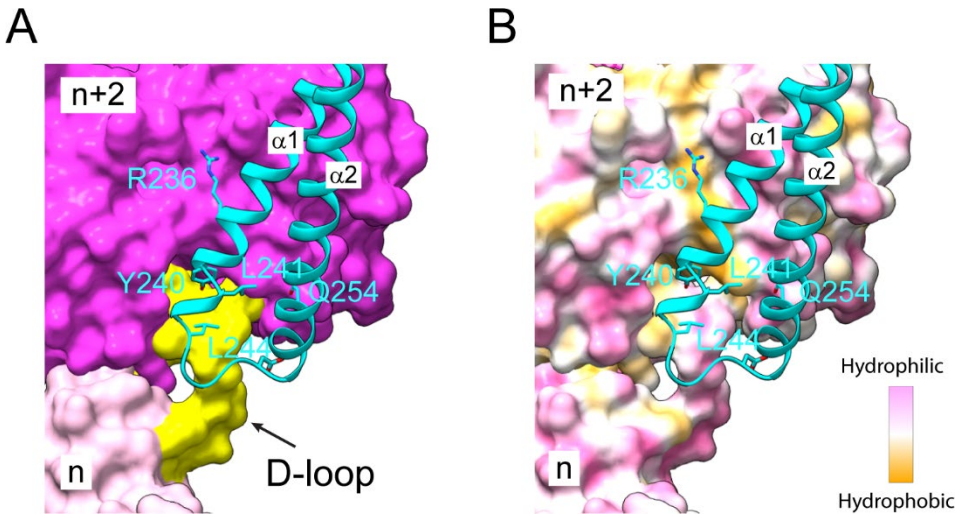

Figure 2 - Figure supplement 3. The interface between Lfat1 ABD and F-actin. (A) Surface representative of two adjacent actin molecules (purple and pink) and the D-loop region of the nth actin molecule is colored yellow. Lfat1 ABD is represented as a ribbon in cyan. Key residues involved in F-actin interaction are shown in sticks. (B) The interface between Lfat1 ABD and F-actin at the same orientation as in (A). The surface of the two actin molecules is colored based on hydrophobicity, with hydrophobic areas in orange and hydrophobic regions in pink.

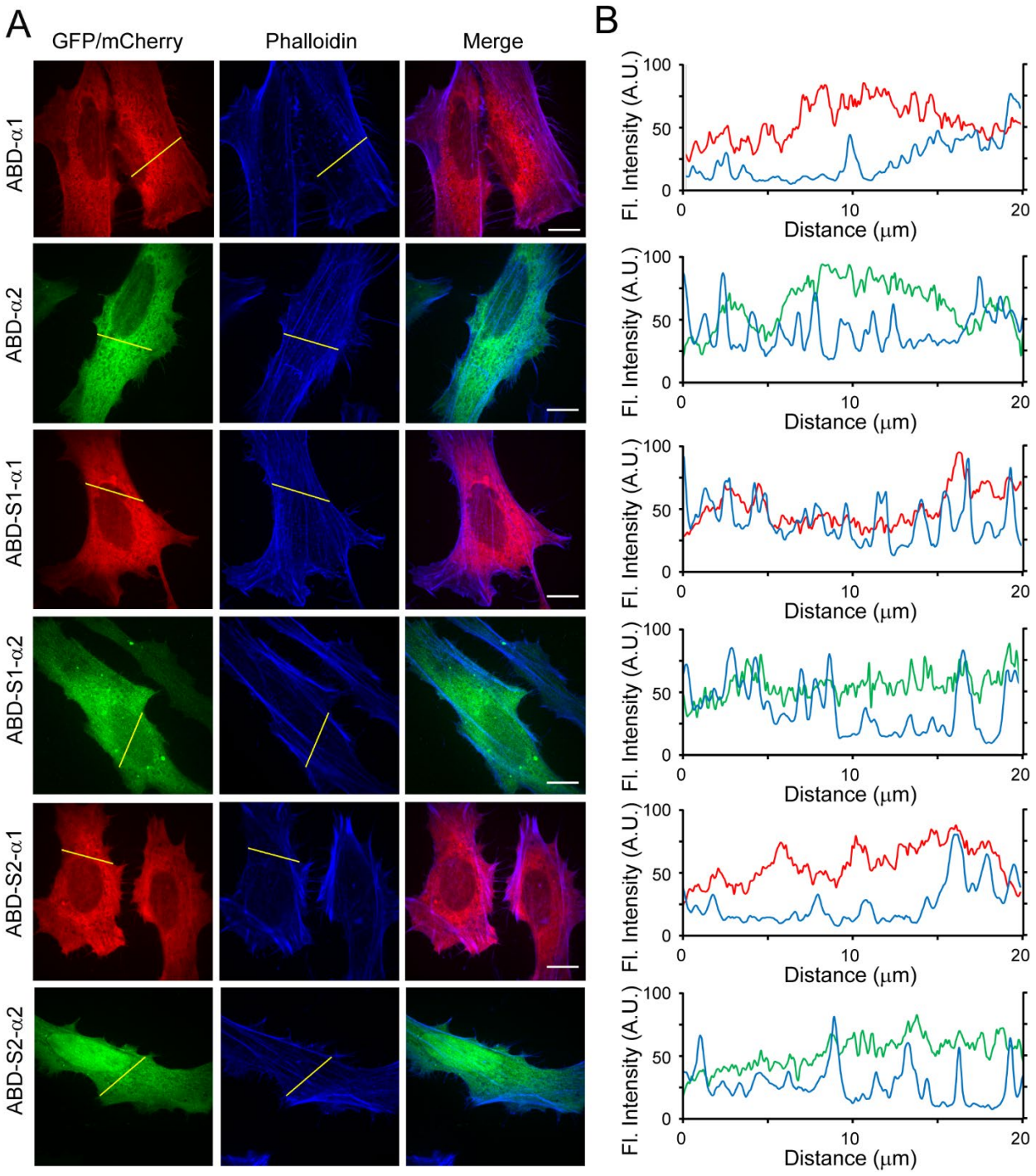

809

810 **Figure 5 - Figure supplement 1. Intracellular localization of separated individual alpha**
811 **helixes of the Lfat1 ABD.** (A) Representative images of HeLa cells transiently expressing
812 individual alpha-helixes from full-length and truncated Lfat1 ABD. Cells were fixed and stained
813 with CF647-phalloidin. (B) Line-scan analysis of constructs tested in (A). Scale bar = 10 μm.

814

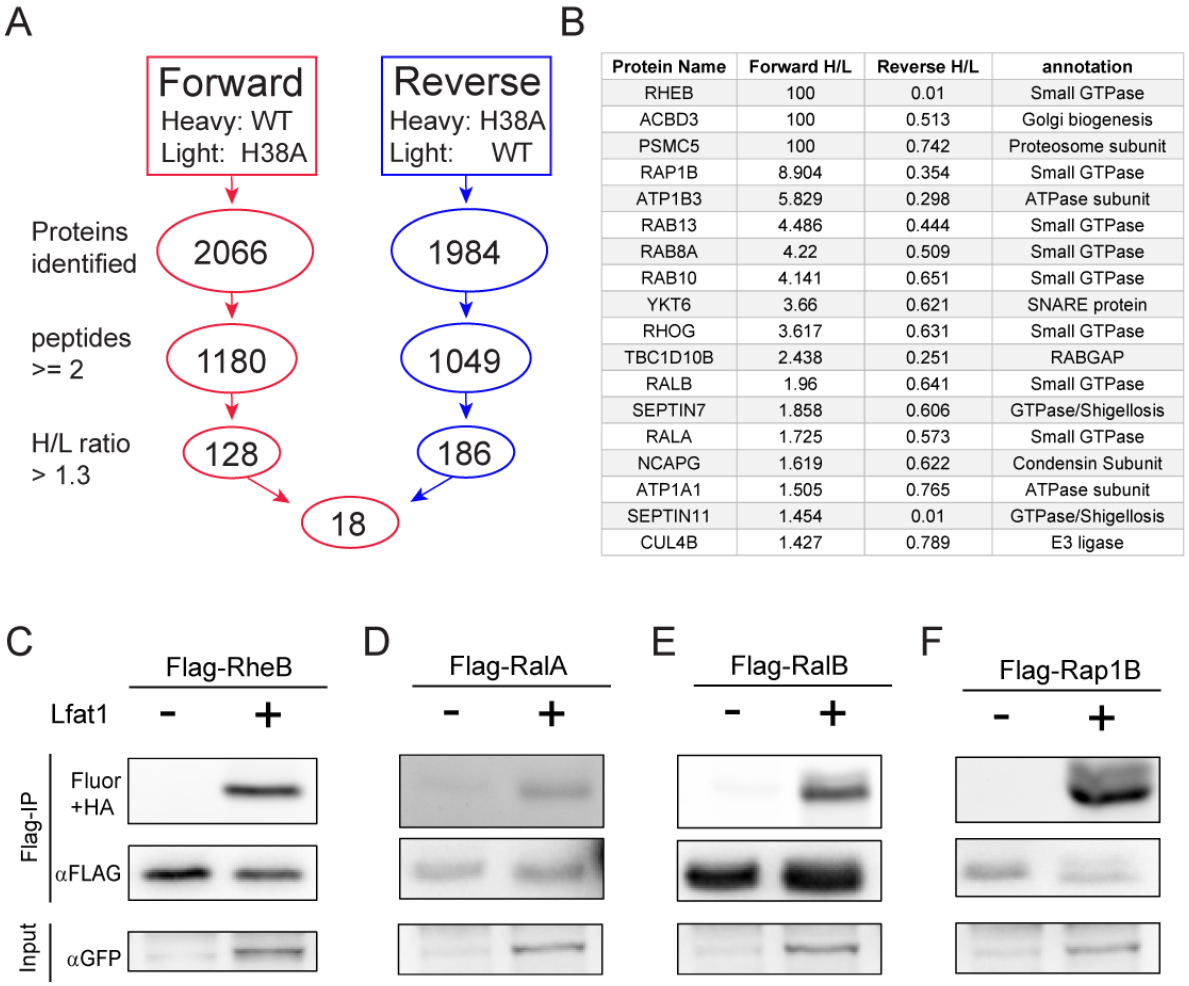

Protein Name	Forward H/L	Reverse H/L	annotation
RHEB	100	0.01	Small GTPase
ACBD3	100	0.513	Golgi biogenesis
PSMC5	100	0.742	Proteosome subunit
RAP1B	8.904	0.354	Small GTPase
ATP1B3	5.829	0.298	ATPase subunit
RAB13	4.486	0.444	Small GTPase
RAB8A	4.22	0.509	Small GTPase
RAB10	4.141	0.651	Small GTPase
YKT6	3.66	0.621	SNARE protein
RHOG	3.617	0.631	Small GTPase
TBC1D10B	2.438	0.251	RABGAP
RALB	1.96	0.641	Small GTPase
SEPTIN7	1.858	0.606	GTPase/Shigellosis
RALA	1.725	0.573	Small GTPase
NCAPG	1.619	0.622	Condensin Subunit
ATP1A1	1.505	0.765	ATPase subunit
SEPTIN11	1.454	0.01	GTPase/Shigellosis
CUL4B	1.427	0.789	E3 ligase

815

816 **Figure 6 - Figure supplement 1. Identification of potential Lfat1 substrates by Click**
817 **chemistry-coupled SILAC mass spectrometry.** (A) Flow chart for selecting high-confidence
818 substrate hits from the SILAC screen. (B) Top hits of potential Lfat1 substrates identified in this
819 SILAC-MS experiment. (C) – (F) Click chemistry verification of some small GTPases selected
820 from the top hit list. N-terminal Flag-tagged RheB, RalA, RalB, or Rap1B was co-expressed along
821 with GFP-Lfat1 or GFP control in HEK293T cells followed by anti-Flag immunoprecipitation and
822 Click chemistry conjugation reaction with an Azide-containing fluorophore. The samples were
823 separated on SDS-PAGE and scanned for fluorescence signals.

824

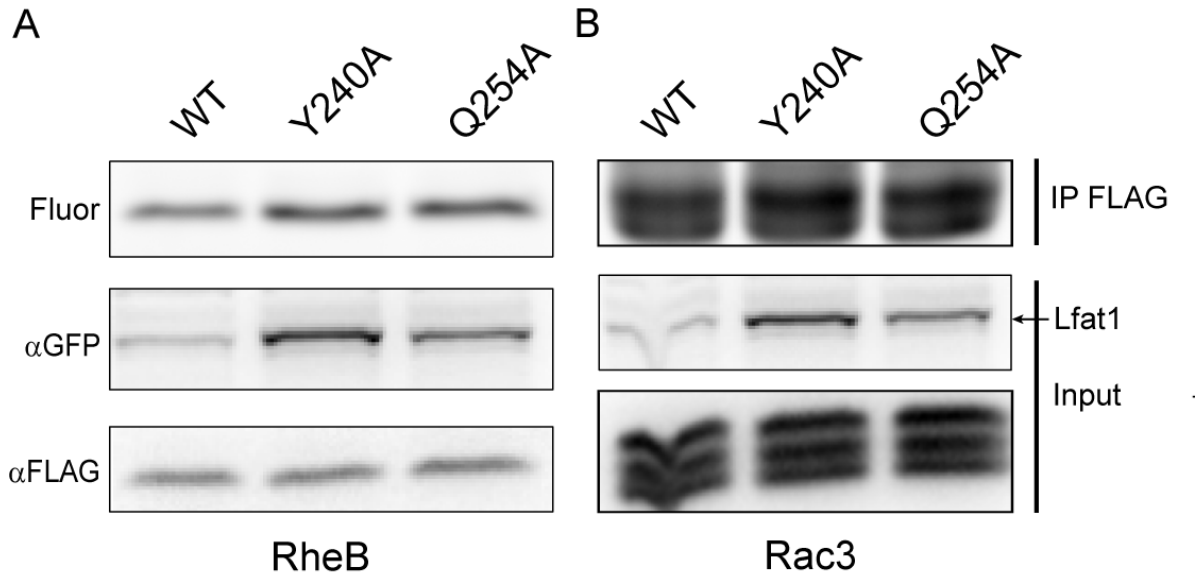

825

826 **Figure 6 - Figure supplement 2. The lysine fatty acyltransferase activity of Lfat1 does not**
827 **dependent on actin binding.** Lfat1 catalyzes lysine fatty acylation of RheB (A) and Rac3 (B). N-
828 terminal Flag-tagged RheB and Rac3 were co-expressed with either GFP-Lfat1 WT, Y240A, or
829 Q254A mutant in HEK293T cells for 24 hours. Flag-RheB and Flag-Rac3 were enriched using
830 immunoprecipitation and subjected to Click chemistry. The samples were then separated on SDS-
831 PAGE and scanned for fluorescence signals or analyzed by Western blot.